

Experiments and computational models to characterize a radiofrequency ablation device for the treatment of rhinitis

by

Faraz Chamani

B.S., Azad University, 2014

A REPORT

submitted in partial fulfillment of the requirements for the degree

MASTER OF SCIENCE

Department of Electrical and Computer Engineering  
College of Engineering

KANSAS STATE UNIVERSITY  
Manhattan, Kansas

2019

Approved by:

Major Professor  
Dr. Punit Prakash

# Copyright

© Faraz Chamani 2019.

## Abstract

Chronic rhinitis is a common health problem described as inflammation of mucous membranes within the nasal cavity. Radiofrequency ablation (RFA) is a minimally invasive therapeutic option for thermal tissue destruction under investigation for treatment of rhinitis. The primary objective of this research is to develop an experimentally validated computational model to guide the design and optimization of RFA devices and systems with application to treating chronic rhinitis. In collaboration with Neurent Medical, we are developing a deployable RFA electrode array for treatment of chronic rhinitis. The impact of RFA device geometry, including electrode length (1.25 mm- 1.75 mm) and inter-pair spacing (3.6 mm- 5 mm), on thermal ablation zones was investigated, and simulation results were experimentally validated by conducting *ex vivo* experiments. Experimental results indicate that increasing electrode length as well as inter-pair spacing within electrode pairs from 1.25 mm to 1.75 mm, and from 3.6 mm to 5 mm respectively, can double the mean depth of ablation from 2 mm to 4 mm (while causing discrete surface ablation zones following RFA). Furthermore, the effects of different energy delivery strategies, including constant power as well as 30% and 60% duty cycle application on ablation results, were investigated through experiments in *ex vivo* tissue. Duty cycled energy delivery may prolong the ablation time depending on applied power level. However, in order to achieve sufficiently deep thermal lesions of 4 mm, thermal damage to tissue surface would be inevitable when using either constant or pulsed energy delivery. The impact of blood perfusion on ablation results was assessed with a computational model. The blood flow effect on ablation zones was negligible within the first 5 s of RFA in superficial regions of 0.5 mm distance from the tissue surface, likely due to a fast heating rate within target tissue. In summary, the computational modeling and experimental results presented in this report

have identified suitable electrode geometry and energy delivery levels for achieving ablation depths of up to 4 mm in the nasal mucosa. These results support the potential of using a deployable RFA electrode for treatment of chronic rhinitis.

# Table of Contents

<b>List of Figures.....</b>	<b>vii</b>
<b>List of Tables .....</b>	<b>x</b>
<b>Chapter 1- Introduction .....</b>	<b>1</b>
Burden of chronic rhinitis .....	1
Radiofrequency ablation .....	2
Objective.....	5
Report outline.....	5
<b>Chapter 2- Radiofrequency Ablation Modeling.....</b>	<b>6</b>
Finite Element Method .....	6
Model geometry .....	7
Equations governing the phenomena .....	9
Initial and boundary conditions.....	11
Assigning material properties .....	13
Tissue electrical conductivity.....	13
Tissue thermal conductivity .....	14
Specific heat capacity of the tissue .....	14
Energy delivery techniques implemented in this work .....	15
Electric current evaluation .....	17
Treatment goals.....	20
<b>Chapter 3- Simulation results .....</b>	<b>21</b>
Impact of electrode length on ablation results .....	21
Impact of inter-pair spacing on ablation results .....	25
Suggested geometry .....	28
<b>Chapter 4- Model verification through experiments .....</b>	<b>32</b>

<b>Chapter 5- Assessment of blood perfusion and energy delivery strategies during radiofrequency ablation .....</b>	<b>41</b>
Blood perfusion impact.....	41
Pulsed energy delivery .....	43
<b>Chapter 6- Conclusions .....</b>	<b>46</b>
<b>References.....</b>	<b>48</b>

## List of Figures

Figure 1: Side view of nasal cavity showing structures inside the nose .....	2
Figure 2: General setup of monopolar radiofrequency ablation .....	4
Figure 3: General setup of bipolar radiofrequency ablation .....	4
Figure 4: Simplified setup and device geometry .....	8
Figure 5: Block diagram of implemented algorithm in the model for power control during radiofrequency ablation.....	16
Figure 6: Modeled cuboid for electric current evaluation.....	18
Figure 7: Simulated electrical parameters based on constant power application.....	19
Figure 8: Simulated changes in tissue impedance during heating for two models with different electrode lengths of 1.25mm and 1.75 mm.....	21
Figure 9: Simulated temperature maps illustrating ablation depth for two models with different electrode lengths of 1.25mm and 1.75 mm.....	23
Figure 10: Simulated temperature maps illustrating surface ablation for two models with different electrode lengths of 1.25mm and 1.75 mm.....	24
Figure 11: Simulated changes in tissue impedance during heating for two models with different inter-pair spacing of 3.6 mm and 5 mm.....	25
Figure 12: Simulated temperature maps illustrating ablation depth for two models with different inter-pair spacing of 3.6 mm and 5 mm.....	26
Figure 13: Simulated temperature maps illustrating surface ablation for two models with different inter-pair spacing of 3.6 mm and 5 mm.....	27
Figure 14: Simulated changes in tissue impedance during heating for the optimized model with electrode length of 1.75 mm and inter-pair spacing of 5 mm.....	28

Figure 15: Simulated temperature maps illustrating ablation depth for two models with different sizes in electrode length and inter-pair spacing (base model with 1.25 mm electrode length and 3.6 mm inter-pair spacing, optimized model with 1.75 mm electrode length and 5 mm inter-pair spacing) .....	29
Figure 16: Simulated temperature maps illustrating surface ablation for two models with different sizes in electrode length and inter-pair spacing (base model with 1.25 mm electrode length and 3.6 mm inter-pair spacing, optimized model with 1.75 mm electrode length and 5 mm inter-pair spacing) .....	30
Figure 17: Neurent Medical deployable RFA device consisting of 6 petals.....	32
Figure 18: CAD illustration for a single petal of the Neurent device containing 5 pairs of electrodes (Picture was demonstrated with the permission of Neurent Medical) .....	33
Figure 19: Experimental setup of radiofrequency ablation including utilized generator and the Neurent device.....	33
Figure 20: Experimental results illustrating impedance roll-off time for two Neurent devices with different geometrical parameters (Blue diamonds and red diamonds represent the performance of optimized device and base device, respectively) .....	35
Figure 21: Experimental results showing ablation depth for two Neurent devices with different geometrical parameters (Blue diamonds and red diamonds represent the performance of optimized device and base device, respectively).....	36
Figure 22: Simulation results vs Experimental results (Performance of device 1 with electrode length of 1.25 mm and inter-pair spacing of 3.6 mm, was compared to performance of device 2 with longer electrode length of 1.75 mm and longer inter-pair spacing of 5 mm).....	37
Figure 23: Changes in electrical parameters during heating in both simulation and experiment .....	38
Figure 24: Thermal ablation zones following ex vivo experiments for device 1 (base device) and device 2 (optimized device with longer electrode length and longer inter-pair spacing).....	39
Figure 25: Simulated changes in tissue impedance for two models with and without blood flow .....	41
Figure 26: Simulation results illustrating blood flow effect on tissue heating rate.....	42

Figure 27: Experimental results showing ablation depth for both pulsed energy delivery and constant power application..... 44

Figure 28: Experimental results showing surface ablation for both pulsed energy delivery and constant power application..... 44

## List of Tables

Table 1: Geometrical parameters of the device and the target tissue.....	9
Table 2: Geometrical parameters of the device used for optimization .....	9
Table 3: Electro-thermal properties of electrodes and insulators utilized in the Neurent device .....	13
Table 4: Summarized simulation findings .....	31
Table 5: Table of heating protocols for constant power application- Ex vivo experiments .....	34
Table 6: Table of heating protocols for pulsed and constant energy deliveries- Ex vivo study .....	43

## Chapter 1- Introduction

Rhinitis is the inflammation of the nasal mucous membrane, which can be accompanied with a number of symptoms such as nasal discharge, watery eyes, sneezing, and stuffy nose caused by nasal congestion <sup>1</sup>. It can be either chronic or acute. Chronic rhinitis will be the focus of this work and can be categorized as either allergic rhinitis, non-allergic rhinitis or mixed rhinitis <sup>2</sup>. Allergic rhinitis (AR) is a common immune system disorder caused by allergens that is usually undiagnosed <sup>3</sup>. Non-allergic rhinitis (NAR) on the other hand, occurs due to an unknown cause, and may include symptoms resembling hay fever, which explains why it is at times similar to allergic rhinitis <sup>4</sup>. To treat the symptoms involved with allergic rhinitis, different medications have been introduced such as nasal corticosteroids, intra nasal antihistamines, decongestants, and leukotriene receptor antagonists. Nevertheless, few of these would be capable of providing complete symptom relief without any complication. Moreover, these medications generally require continuing administration each day, which may impact the life quality of patients <sup>5</sup>.

### Burden of chronic rhinitis

Although many people underestimate rhinitis symptoms and treat it as an inconvenience instead of an illness, its economic impact could be significant. In the United States, direct medical costs of rhinitis were reported as US\$ 6.1 billion in 2000, which doubled to US\$ 11.2 billion in five years <sup>6</sup>. Furthermore, the burden of indirect costs, including work inefficiency and missed days of school or work, should be considered. Hence, this medical condition not only impacts physical functioning of patients but also affects the financial burden of society. Non-allergic rhinitis in contrast, involves around one-fourth of rhinitis related cases and affects up to 30 million people in the United States <sup>7</sup>. If conservative medical cares do not provide sufficient symptoms relief,

operative treatment of inferior nasal concha would be considered. However, available treatments such as partial or complete conchotomy, laser reduction of mucous membrane, and cryosurgery are usually followed with bleeding, pain and desiccation of nasal cavity<sup>8</sup>. **Figure 1** describes the side view of the nasal cavity showing structures within the nose.

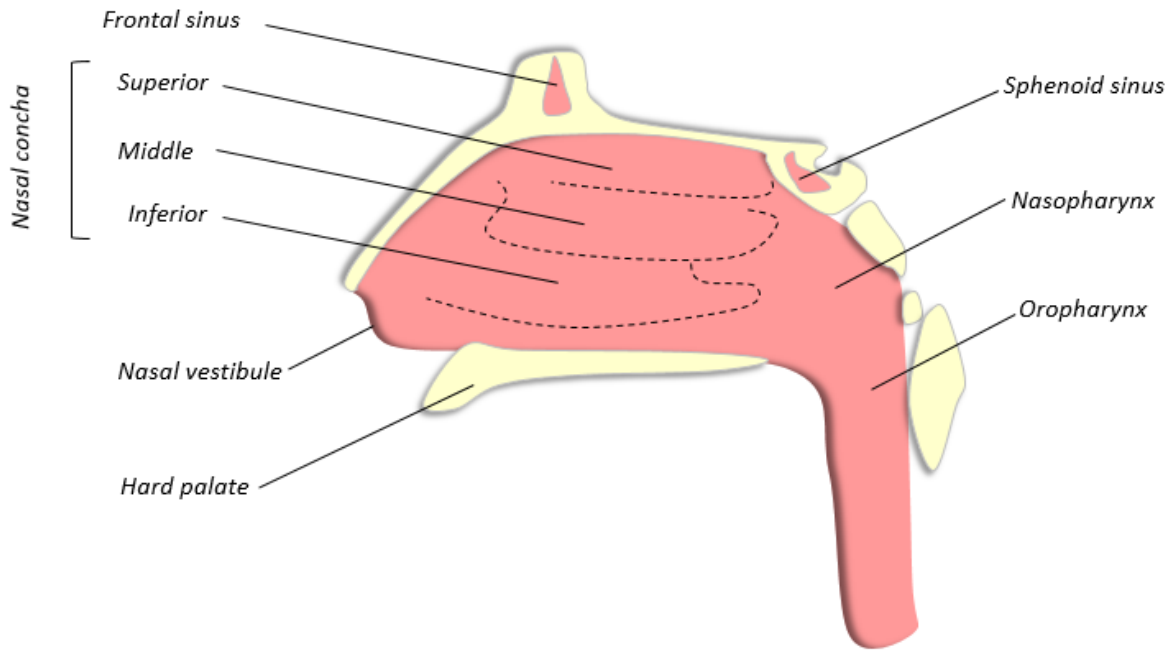


Figure 1: Side view of nasal cavity showing structures inside the nose

## Radiofrequency ablation

Radiofrequency energy delivery for provoking tissue destruction has been the main focus of this work. Radiofrequency ablation (RFA) is a minimally invasive therapeutic method used for various purposes such as catheter ablation, destruction of tumors or the nerve fibers responsible for conveying pain signals to the central nervous system<sup>9</sup>. Radiofrequency ablation devices operate in frequencies ranging from 460 kHz to 550 kHz and can cause tissue thermal damage by creating friction heating in the target zones. The heat is generated by movement of ions as they

follow the trend in a high frequency electric current dispersed from electrode tip to the surrounding area <sup>10</sup>. As ablation time passes, and tissue temperature rises above 60°C, intracellular protein denaturation occurs that would be accompanied with cells death and a subsequent coagulated region within the living tissue <sup>11</sup>. Higher temperature rises could be associated with changes in tissue material properties caused by water evaporation and tissue charring. These changes in tissue physical characteristics may adversely affect cell death progression within the target tissue <sup>12</sup>. For instance, at temperatures above 100°C, tissue begins producing gas which requires lots of energy to convert liquid within the tissue to gas. Consequently, tissue charring happens and causes a dramatic rise in tissue impedance which will indeed limit heating rate within the target zones <sup>13</sup>.

According to a research conducted by Kezirian et al. <sup>14</sup>, around one hundred thirty cases with sleep disordered breathing (SDB) issues were treated by temperature-controlled radiofrequency ablation in the inferior concha without any serious complications. Hereby, radiofrequency ablation technique may have the potential to be used as one of the least risky therapeutic approaches for treating nasal disease.

Radiofrequency energy is generally delivered in either monopolar or bipolar electrode configurations. In the case of monopolar radiofrequency ablation, electrical current is flowing between active electrode and the corresponding returning pad. This system configuration, however, might bring some complications including but not limited to heat retention and subsequent perspiration within the patient's body <sup>15</sup>. In contrast to monopolar configuration, a more localized approach to deliver RF energy, would be bipolar or multipolar electrode configurations <sup>16</sup>. During a bipolar RFA, electrical current flows within a considerably short path between two active and ground electrodes, thus a more localized heating is achieved. **Figures 2**

and **Figure 3** illustrate the general setups for monopolar and bipolar radiofrequency ablation, respectively.

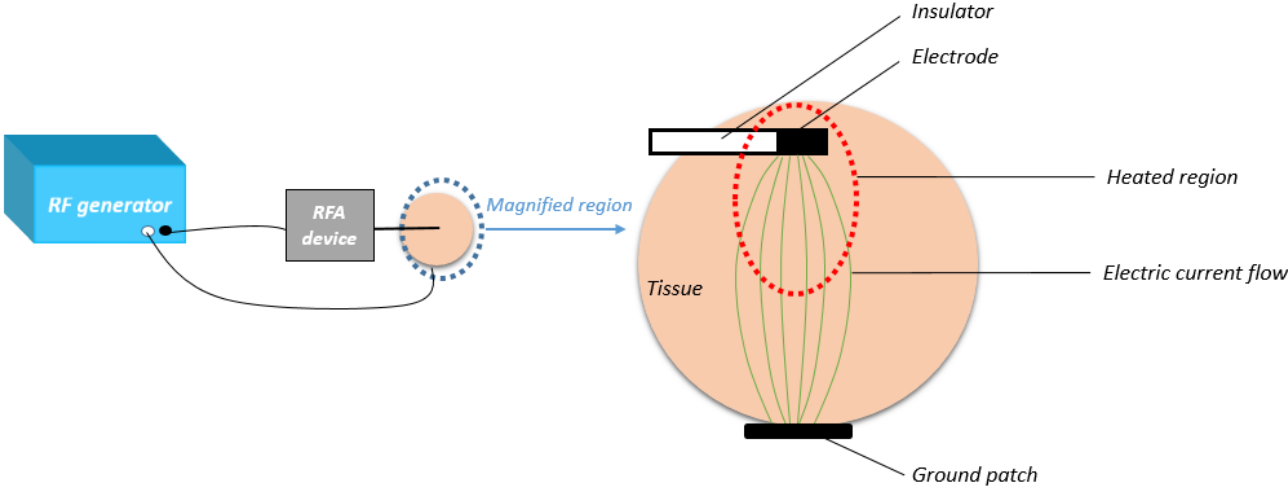


Figure 2: General setup of monopolar radiofrequency ablation

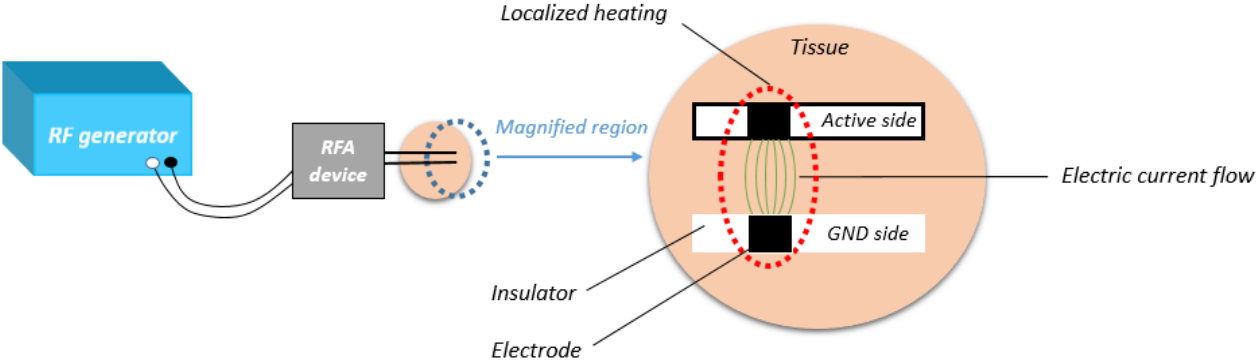


Figure 3: General setup of bipolar radiofrequency ablation

As shown in **Figure 3**, limited route of electrical current would create a more localized thermal injury within the tissue when compared to **Figure 2** that shows a monopolar RFA setup. In this study, a ready-made RF generator capable of constant power delivery was utilized, and a bipolar RFA device (Neurent Medical, Galway, Rep. of Ireland) consisting of 6 petals each containing 5 pairs of active and return electrodes placed on two parallel wires. This study builds on an earlier work between Kansas State University and Neurent Medical which discussed the feasibility of radiofrequency ablation for rhinitis treatment <sup>17</sup>.

### Objective

In order to comprehensively evaluate various impacts of geometrical and electrical parameter on ablation results while avoiding a considerable number of experiments and constructions in the design phase, a primary objective of developing an experimentally verified computational model was aimed in this work. This model would be capable of predicting ablation results with respect to different inputs ranging from device geometry to energy delivery selection. The introduced RFA system can be used for treatment of chronic rhinitis by interrupting autonomic function within the mucosal structures.

### Report outline

The rest of report is organized as follows:

- **Chapter 2** begins with a brief review in RFA computer modeling and introduces the modeling techniques implemented in this work.
- **Chapter 3** investigates detailed impacts of RFA device geometrical parameters on ablation zones formation by FEM simulations.
- **Chapter 4** will experimentally verify the FEM simulation results presented in chapter 3.

- **Chapter 5** investigates possible impacts of blood flow and energy delivery strategies on ablation results through computation and bench studies, respectively.
- **Chapter 6** will include conclusions, and suggestions for future research studies.

## **Chapter 2- Radiofrequency Ablation Modeling**

RFA computational modeling can play an important role in the development of medical systems. Numerical simulations are capable of predicting the electric field intensity, current pathway within the tissue, and the resulted thermal damage following RFA simulations. Computational models can be very helpful specifically during the design phase due to:

- 1- Reducing number of experiments and faster development
- 2- Comprehensive evaluation of various parameters involved in the system
- 3- Lowering related costs
- 4- Convenience (No need for providing specific fresh tissue)

### **Finite Element Method**

Finite element method (FEM), is known as a numerical method capable of solving partial differential equations in mathematical physics such as Heat transfer and Laplace's equations. It is one of the most widely used computational method in RFA modeling. Gao et al.<sup>18</sup> investigated the effects of electro-thermal parameters on radiofrequency ablation results. Wang et al.<sup>19</sup> studied the correlation between lesions size and the treatment time during radiofrequency ablation. Tian et al.<sup>20</sup> established a treatment planning to predict therapeutic parameters accurately by radiofrequency ablation (RFA) in spinal tumor. Trujillo and Berjano<sup>21</sup>, also

investigated the mathematical functions used to describe temperature dependence of electrical and thermal conductivities in RFA models.

COMSOL Multiphysics was employed in this study to predict thermal ablation zones following different energy delivery strategies. Also, the impacts of geometrical parameters of device on ablation results has been analyzed.

### Model geometry

Geometrical modeling of RFA such as specific electrode configurations, detailed electrode shapes, and the specific tissue layers could be very complex, leading to longer computation time. Therefore, it would be helpful in some cases to consider reasonable geometrical simplifications in the model that can bring less computational burden. These simplifications could be involved with reducing the number of electrode pairs or sometimes avoiding unnecessary geometrical details of the target tissue while considering essential parts that could have impact on simulation results. In this work, a 3D computational model was implemented that is consisting of different domains: liver tissue, air, electrodes, and insulators. Model geometry explains two cylindrical wires each containing two hemi-cylindrical electrodes were placed on a cuboidal liver tissue.

To better understand the RFA device geometry modeled in this study, different perspectives of the whole setup including device's geometrical parameters are shown in **Figure 4**.

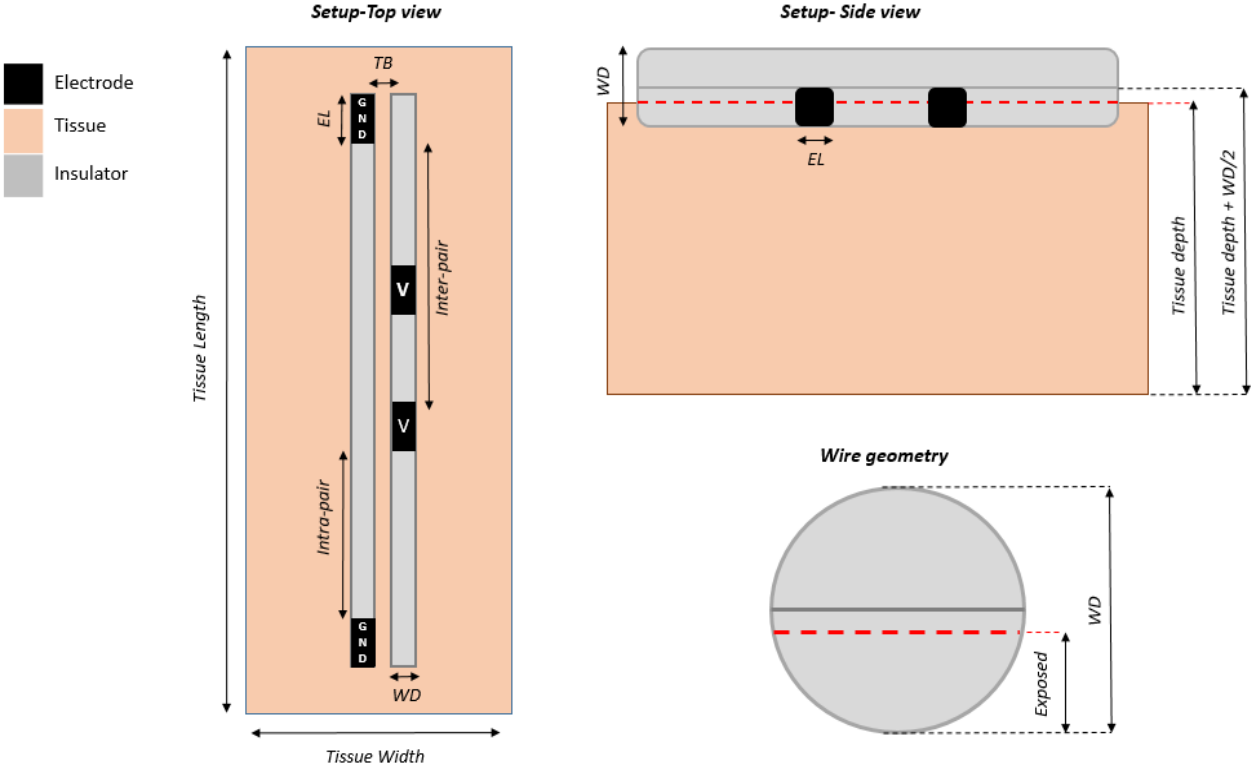


Figure 4: Simplified setup and device geometry

The values for both fixed and variable geometrical parameters used in model are shown in **Table 1** and **Table 2**.

Table 1: Geometrical parameters of the device and the target tissue

<b>Fixed</b> parameters	Value (mm)
WD	0.2
Tissue depth	40
Exposed	0.07
TB	0.1
Tissue length	20
Tissue width	14
Intra-pair	1.15

Table 2: Geometrical parameters of the device used for optimization

<b>Variables</b>	Initial value (mm)
EL	1.25
Inter-pair	3.6
<b>Variables</b>	Second value (mm)
EL	1.75
Inter-pair	5

Tetrahedral mesh elements with the total number of 432159 were generated within all model domains with minimum and maximum element size of 0.08 mm and 0.4 mm respectively in the target tissue. Finest mesh density was selected in electrode domains (with maximum element size of 0.06 mm) since the electro-thermal gradients are tend to be steep in these regions.

### Equations governing the phenomena

Radiofrequency ablation models can be implemented based on the time domain solver of a coupled electrical-thermal problem<sup>22</sup>. RFA modeling in this study was accompanied with two partial differential equations for solving electric field and temperature distribution respectively governed by Laplace's equation and Pennes' Bioheat equation. In addition, an ordinary differential equation governed by Arrhenius model was implemented in order to calculate the accumulating thermal damage during RFA simulation, to provide necessary feedback for electrical conductivity behavior.

Distributed heat source  $Q_{JH}$  (Joule loss) is calculated by the scalar product of current density and electric field intensity,

$$Q_{JH} = \mathbf{J} \cdot \mathbf{E} \quad (\text{Eq. 1})$$

where  $\mathbf{J}$  is the current density [ $\text{A}/\text{m}^2$ ] and  $\mathbf{E}$  is the electric field intensity [ $\text{V}/\text{m}$ ].

The values of these two vectors are evaluated using Laplace's equation,

$$\nabla \cdot [\sigma(T, t)\nabla V] = 0 \quad (\text{Eq. 2})$$

where  $V$  and  $\sigma(T, t)$ , indicate the applied voltage [ $\text{V}$ ] and tissue electrical conductivity [ $\text{S}/\text{m}$ ], respectively.

The next part of simulation would solve a partial differential equation with the purpose of calculating spatial distribution of temperature within tissue:

$$\nabla \cdot K(T)\nabla T + Q_{JH} - Q_p + Q_m = \rho c \frac{\partial T}{\partial t} \quad (\text{Eq. 3})$$

where  $\rho$  is tissue mass density [ $\text{kg}/\text{m}^3$ ],  $K(T)$  is temperature dependent thermal conductivity of the tissue [ $\text{W}/(\text{m}\cdot\text{K})$ ],  $c$  is tissue specific heat capacity [ $\text{J}/(\text{kg}\cdot\text{K})$ ],  $T$  is the temperature (K),  $Q_{JH}$  is the resistive loss [ $\text{W}/\text{m}^3$ ] calculated from **Eq. 1**, and  $Q_m$  is metabolic heat generation within the tissue [ $\text{W}/\text{m}^3$ ] that is usually ignored since it has negligible impact on temperature distribution when compared to other terms<sup>23</sup>.

Finally,  $Q_p$  represents the heat loss caused by blood perfusion within living tissue. This term can be calculated as shown below:

$$Q_p = \rho_b \omega_b(T) c_b (T - T_b) \quad (\text{Eq. 4})$$

Where  $\rho_b$  indicates the mass density of blood [ $\text{kg}/\text{m}^3$ ],  $\omega_b$  represents the velocity of blood perfusion within target tissue [ $\text{s}^{-1}$ ],  $c_b$  is the blood heat capacity [ $\text{J}/(\text{kg}\cdot\text{K})$ ], and  $T_b$  represents blood temperature that was considered as  $37\text{ }^\circ\text{C}$  in the model.

Perfusion heat loss can play an effective role in coagulated zones within the tissue during radiofrequency ablation. However, this term would be considered as zero in *ex vivo* RFA modeling due to existence of no blood flow within excised tissue.

In this study, in order to predict the boundaries of tissue thermal damage after exposing them to a particular heating protocol, an Arrhenius cell death model was implemented as expressed in **Eq.5** which is based on the first order kinetics, and could be used for predicting tissue damage parameter shown as  $\Omega(T, \tau)$  following RFA:

$$\Omega(T, \tau) = \int_0^\tau A e^{\left(\frac{-E_a}{R \cdot T(t)}\right)} dt \quad (\text{Eq. 5})$$

where  $A$  indicates frequency factor [ $\text{s}^{-1}$ ],  $E_a$  is activation energy [ $\text{J}/\text{mol}$ ],  $T(t)$  represents time dependent absolute temperature [ $\text{K}$ ] within tissue, and  $R$  is the gas constant ( $8.314\text{ }[\text{J}/(\text{mol}\text{ K})]$ ). Similar to <sup>24</sup>, in order to estimate whitened thermal ablation zones within target tissue, optimized values of  $A$  and  $E_a$  as  $5.51 \times 10^{41}\text{ }[\text{s}^{-1}]$  and  $2.769 \times 10^5\text{ }[\text{J}/\text{mol}]$ , were implemented in the model, respectively. Finally, estimation of thermal damage was accomplished based on a threshold of  $\Omega(T, \tau) = 1$ , indicating 63% probability of cell death within heated tissue.

### Initial and boundary conditions

An initial source voltage ( $V_0 \neq 0$ ) was applied to the boundaries of the active electrodes. In contrast, the corresponding electrodes were defined as electrical ground returns ( $V = 0$ ).

The electric fields may be quite high in insulator domains, however, electrical current would be essentially zero. Thereby, electric insulation condition was applied on insulator boundaries meaning that electric current density would be divergence free, and consequently no electrical current passes through non-conducting surfaces,

$$\nabla \cdot \sigma(T, t) \nabla V = 0 \quad (\text{Eq. 6})$$

where  $\sigma(T, t)$  and  $V$  represent electrical conductivity [S/m] and electric potential at non-conducting surfaces [V], respectively.

The electrodes are highly conductive, and according to *Eq. 1*, these domains experience quite a negligible heating when compared to surrounding tissue due to a very small electric field.

Hence, these domains were omitted from this electrical model. Likewise, since the insulators are perfectly non-conducting meaning zero electrical current, again the heating would be negligible.

These domains were also removed from electrical model.

Convective Heat Flux boundary condition shown in *Eq. 7* was applied to the exterior surface of modeling domain.

$$\mathbf{n} \cdot \mathbf{k} \nabla T = h(T_{ext} - T) \quad (\text{Eq. 7})$$

Heat transfer coefficient and external temperature ( $T_{ext}$ ) were selected as 10 [W/(m<sup>2</sup>·K)] and 28 °C, respectively to reasonably approximate free convective cooling. The implemented boundary condition reasonably approximates free convective cooling within tissue. Also, a more conservative boundary condition on external surfaces would be Thermal Insulation boundary condition meaning that tissue is perfectly insulated from external environment.

## Assigning material properties

Solving governing equations necessitates to assign material properties of target tissue as well as the applicator. **Table 3** includes implemented material properties of the device introduced by Neurent Medical.

*Table 3: Electro-thermal properties of electrodes and insulators utilized in the Neurent device*

Part	Material	Thermal conductivity [W/m.K]	Electrical conductivity [S/m]	Heat capacity [J/Kg·K]	Density [Kg/m <sup>3</sup> ]
Electrode	Nitinol	17.99	$1.2 \times 10^6$	3503	6450
Insulator	Parylene	0.084	$1 \times 10^{-14}$	2977	1289

Tissue electrical and thermal characteristics can considerably change with respect to time and temperature. Next section includes tissue (liver) material properties implemented in the model.

### Tissue electrical conductivity

Arrhenius model was utilized to simulate a relatively realistic behavior of tissue electrical conductivity which is affected by both time and temperature. *Eq. 8* extracted from <sup>25</sup>, shows thermal damage consideration of the electrical conductivity function implemented in the model,

$$\sigma(T, t) = \sigma_{37} [1 + \alpha(T - 37) + \beta u(t) - \gamma(T - 37)^8] \quad (\text{Eq. 8})$$

where  $T$  is temperature [ $^{\circ}\text{C}$ ], and  $\sigma_{37}$  is the tissue electrical conductivity at  $37^{\circ}\text{C}$ . The modeled target tissue was chosen to be liver, and the initial electrical conductivity was chosen as  $0.29$  [ $\text{S/m}$ ].

$\alpha$ ,  $\beta$ , and  $\gamma$  are optimized model parameters. Similar to <sup>25</sup>, for monitoring changes in tissue electrical conductivity, the following set of parameters were implemented:

$$\alpha = 1.26 \times 10^{-2} [^{\circ}\text{C}^{-1}], \beta = 1.25, \text{ and } \gamma = 2.0 \times 10^{-15} [^{\circ}\text{C}^{-8}].$$

### Tissue thermal conductivity

Trujillo & Berjano <sup>21</sup>, investigated different thermal conductivity functions at radiofrequency range, and concluded that ignoring temperature dependency of thermal conductivity is reasonable, meaning that a constant value could be used. However, a more realistically used estimation of liver tissue thermal conductivity includes a linear growth at temperatures below  $100^{\circ}\text{C}$ , while maintaining a constant value for temperatures above  $100^{\circ}\text{C}$  <sup>26</sup>. Below, describes the temperature dependent thermal conductivity function that was utilized in the model.

$$k(T) = k_{20} + 0.0008 T \quad (\text{Eq. 9})$$

Where,  $k_{20} = 0.498$  [ $\text{W}/(\text{m}\cdot\text{K})$ ] is the thermal conductivity at  $20^{\circ}\text{C}$ , and  $T$  represents temperature range up to  $100^{\circ}\text{C}$  <sup>25</sup>.

### Specific heat capacity of the tissue

Tissue heat capacity can be influenced by temperature rise during RFA. For instance, at  $T=100^{\circ}\text{C}$ , the latent heat would be required for water evaporation, and hence, a significant rise in tissue specific heat capacity will be inevitable. Temperature dependence of tissue specific heat capacity is usually eliminated in RFA modeling <sup>27</sup>. However, Haemmerich et al. <sup>28</sup>, reported a growing

behavior of the heat capacity between 65 °C and 83.5 °C, while maintaining a constant value at temperatures below 65 °C. Therefore, similar to <sup>25</sup>, a piecewise function was implemented for simulating the behavior of heat capacity during radiofrequency ablation,

$$\begin{aligned} c(T) &= c_0 + k_c(T - 63.5) & T > 63.5 \text{ }^\circ\text{C} & \quad (\text{Eq. 10}) \\ c(T) &= c_0 & T \leq 63.5 \text{ }^\circ\text{C} & \end{aligned}$$

Where,  $c_0$  is the initial specific heat capacity of liver tissue set as 3800 [J/(kg·K)], and  $k_c$  is the fitting parameter with value of 28.9 [J/(kg·K<sup>2</sup>)].

### Energy delivery techniques implemented in this work

Various modes of radiofrequency energy delivery have been previously reported such as power-controlled mode ( $P = c$ ), temperature-controlled mode ( $T = c$ ), and impedance-controlled mode ( $Z < c$ ) <sup>29</sup>.

The RF generator used in this work functions in constant power mode. Thereby, constant power radiofrequency ablation was simulated to study lesion zone formation with respect to ablation time, applied power level, and device geometry. In a previous study constant power RFA was simulated by applying a Dirichlet electric boundary condition at the active electrode corresponding to a particular level of power from the generator <sup>30</sup>. However, in clinical practices, such energy delivery modeling might not accurately simulate a constant power application due to the fact that tissue electrical conductivity changes with respect to temperature rise and ablation time. The voltage at the ablating electrode could be adjusted with regards to changes in current density in order to maintain the applied power within an acceptable range. In another study, the applied voltage at the active electrode was manually reduced with respect to time for maintaining

power level <sup>31</sup>. This modeling technique, however, may not be very helpful if there would be no access to transient voltage data from the generator.

In this work, a closed loop bang-bang control system is introduced that automatically regulates the applied voltage with the purpose of constant power delivery. To begin with, the initial applied voltage level was preselected based on the simulated power level at the very beginning. Then, an implicit Events interface was implemented to stop the time-stepping algorithms at a chosen output threshold happening at an unknown time, and offer the possibility of altering voltage input value. **Figure 5** describes the closed loop control system implemented in the model,

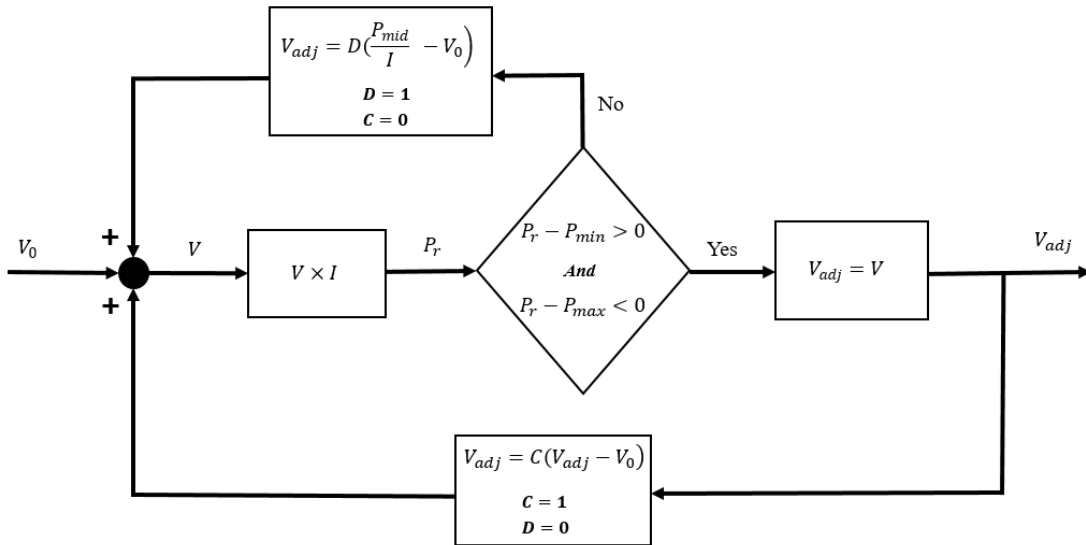


Figure 5: Block diagram of implemented algorithm in the model for power control during radiofrequency ablation

where  $V_0$  represents the initial applied voltage [V] as the input,  $I$  is the total electrical current [A],  $P_r$  is the real power [W] calculated during simulation,  $P_{min}$  is the down threshold set for Power level,  $P_{max}$  is the up threshold set for Power level,  $P_{mid}$  indicates any number chosen

within the specified power range ( $P_{min} < P_{mid} < P_{max}$ ), and finally,  $V_{adj}$  is the adjusted voltage [V] continuously getting updated during simulation to maintain the power level ( $P_r$ ).

### Electric current evaluation

In order to evaluate the total electric current during simulation as an indicator for input voltage, current density was treated as a vector, and the total dispersed electric current was obtained by summing up surface integration (*Eq. 11*) of current densities normal to each surface surrounding the ablating electrodes:

$$I = \int J \cdot dS \quad (\text{Eq. 11})$$

According to the geometry of the model, a cuboid encompassing one active electrode was defined in order to calculate total current flowing from one active electrode through all surfaces around it as shown in **Figure 6**. The width and depth of cuboid both were selected as the value of wire radius, and the length of cuboid was chosen as 1.2 times of the electrode length. Then, that value was multiplied by total number of active electrodes used in the model accounting for the total electric current flowing in the tissue.

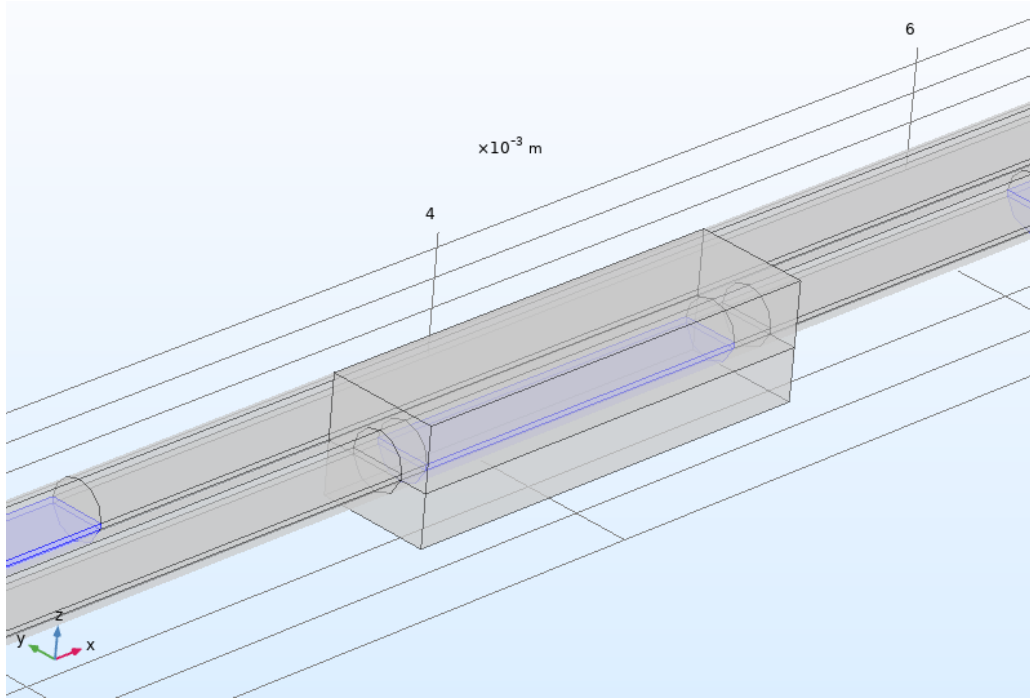


*Figure 6: Modeled cuboid for electric current evaluation*

This method will allow us to automatically maintain the power level with respect to changes in electrical current caused by tissue electrical conductivity during RFA simulation.

Simulated electrical parameters are shown in **Figure 7** based on described technique for maintaining power level during RFA simulation.

Discrete States interface was used in this work to define the state of applied power. Then, two Indicator States were implemented that together define a closed loop control system for the output power level depending on the total current dispersed from active electrodes. Finally, the event is triggered through implicit events when the logical condition becomes true. Once this happens, the transient solver stops and restart with the newly initialized input voltage in this model.

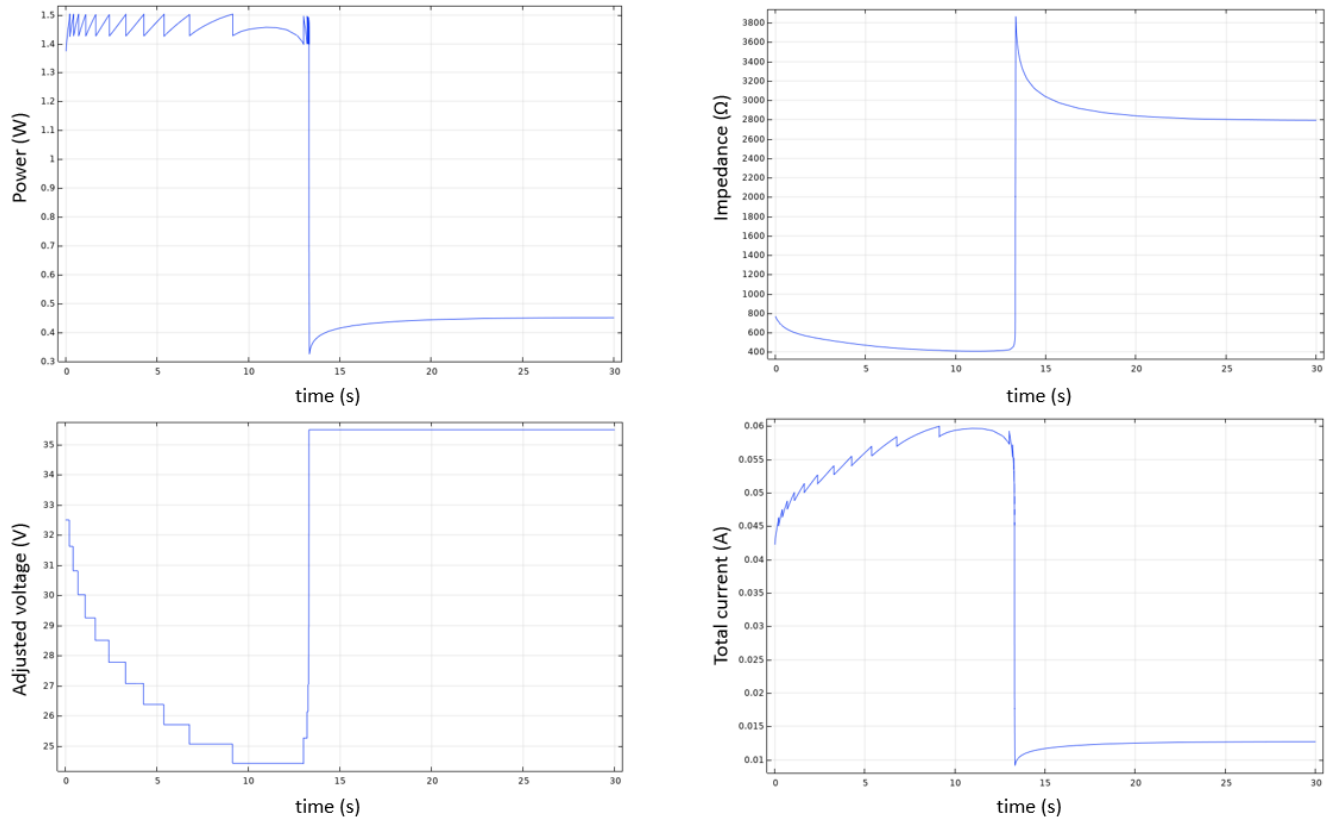


Figure 7: Simulated electrical parameters based on constant power application

As shown in the power plot, the applied power was maintained constant with less than 5% tolerance. This indicates the capability of the described method for modeling constant power application during radiofrequency ablation. Keep in mind that this simulation was based on a constant power application of 1.5 W for 30 seconds.

Impedance roll-off happened almost in 15 seconds, and before that, the applied voltage was decreasing to maintain the power level by compensating for continuously increasing electric current. However, this adjustment was done up to a certain point where cell damage starts occurring and electrical conductivity begins to drop associated with a dramatic decrease in electrical current.

After impedance roll-off, applied voltage again should be adjusted to maintain the power level but this time it has to increase since electric current starts decreasing. The adjusted voltage will be eventually surpassed by a significant drop in electric current value, and the output power level will jump out of the implemented control loop meaning end of simulation due to impedance roll-off.

### Treatment goals

The optimal clinical goals of rhinitis treatment following radiofrequency ablation are clarified:

- 1- Achieving sufficiently large ablation depth (4mm depth of ablation suggested by Neurent Medical)
- 2- Avoiding or minimizing surface damage within nasal cavity that might cause complications following treatment
- 3- Not a very long treatment time for surgeon's convenience and patient's safety

Therefore, simulations were done to help us comprehensively evaluate and understand the relationship between different input parameters and the subsequent ablation zones. However, the optimal clinical goals mentioned above, made us to introduce a RFA device based on simulation results analysis.

## Chapter 3- Simulation results

The primary purpose of this chapter will be to simulate the performance of a bipolar RFA device with regards to various geometrical configurations. The impact of device geometry on ablation results will be investigated.

### Impact of electrode length on ablation results

For the first part of simulation, the impact of electrode length on ablation results was assessed based on constant power application while keeping all other geometrical parameters fixed. Also, the applied power was maintained in the same level for both models.

The model with longer electrode length led to a longer ablation time due to causing a considerable delay in impedance roll-off time. Thereby, same amount of power was applied for longer time which means more energy delivery to the target tissue and thereby larger ablation zones were created in the model with longer electrode length. **Figure 8** shows the comparison of impedance behavior between the two models.

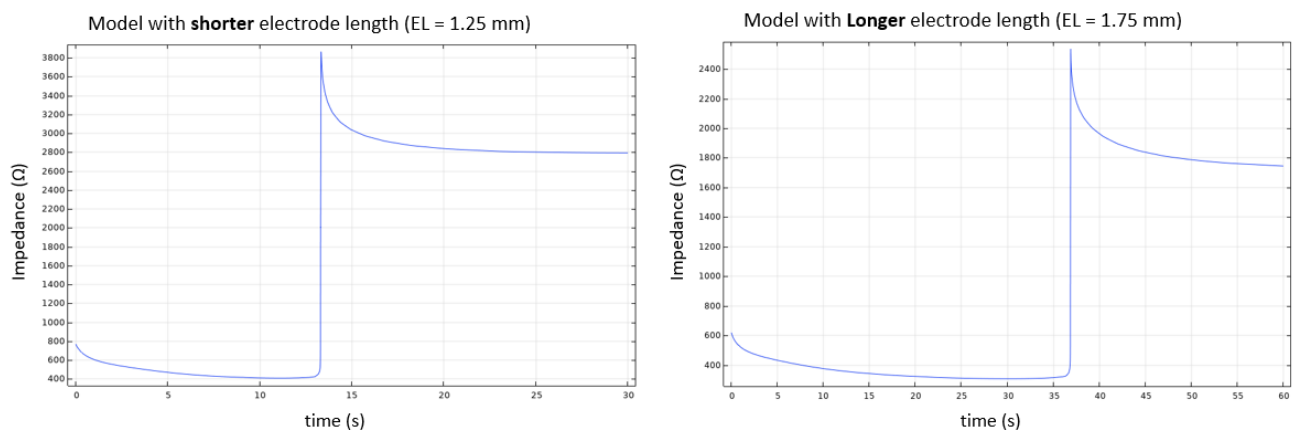


Figure 8: Simulated changes in tissue impedance during heating for two models with different electrode lengths of 1.25mm and 1.75 mm

It is interesting that there was a decrease in impedance values for the model with longer electrode length which could be likely due to more involved tissue within electrode pairs and eventually more thermal conductivity can be involved in cooling down the heated parts. This can cause the voltage to decrease in order to maintain the same amount of power ( $P = V^2/R$ ). On the other hand, the total electrical current should increase to compensate for the decrease in voltage level. Keep in mind that electrical conductivity behavior is affected by temperature gradient and thermal damage in each time step which explains why electrical parameters are continuously changing during RFA. **Figures 9** shows the temperature maps ( $^{\circ}\text{C}$ ) and thermal damage contours for both models following RFA.

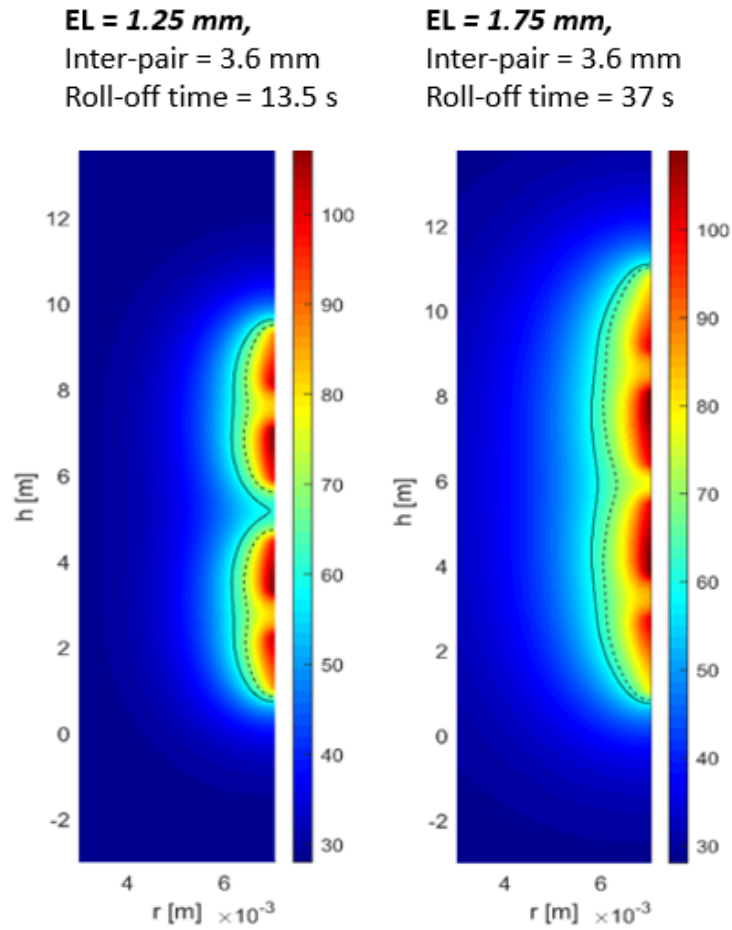
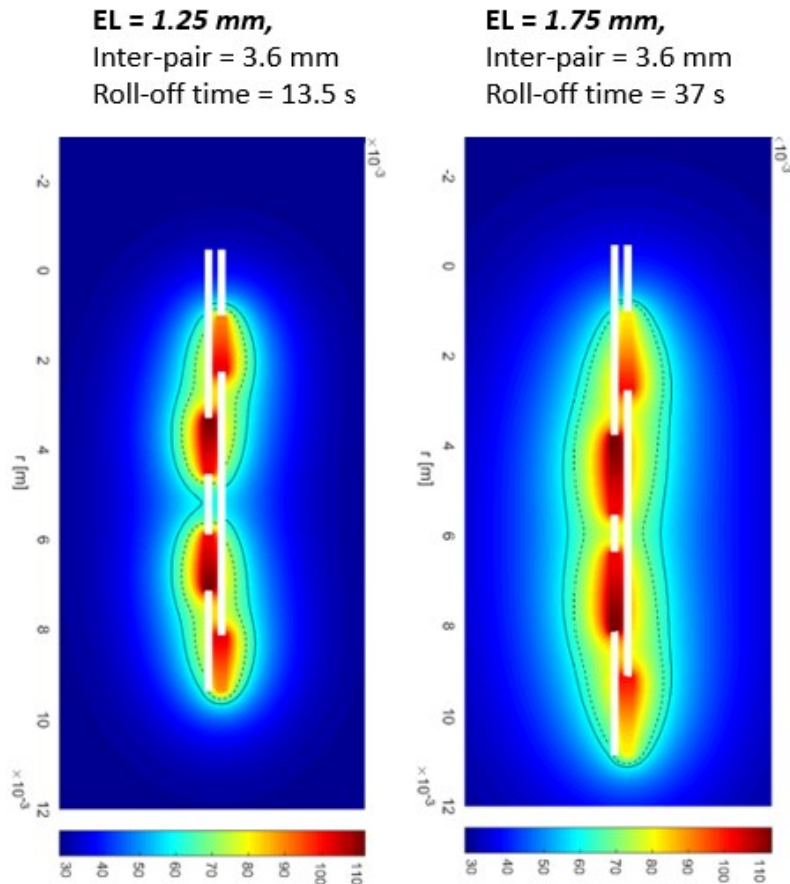


Figure 9: Simulated temperature maps illustrating ablation depth for two models with different electrode lengths of 1.25mm and 1.75 mm

Ablation results with a longer electrode length shows a larger ablation depth. Depth of ablation increased from 0.5 mm to 1 mm when using a longer electrode length. Surface lesions are reported in **Figure 10**.



*Figure 10: Simulated temperature maps illustrating surface ablation for two models with different electrode lengths of 1.25mm and 1.75 mm*

Simulation results show a considerable increase in lesion sizes both in depth and surface of target tissue for the model with longer electrode length. Thereby, electrode length variation can significantly impact the lesion size during RFA.

## Impact of inter-pair spacing on ablation results

Again, for this part of simulations, the impact of one specific geometrical parameter (inter-pair) on ablation results was investigated based on the same power level while keeping all other geometrical parameters fixed.

There was no difference in total ablation time since the impedance roll-off happened almost at the same time for both cases. **Figure 11** shows the comparison in tissue impedance behavior between the models.

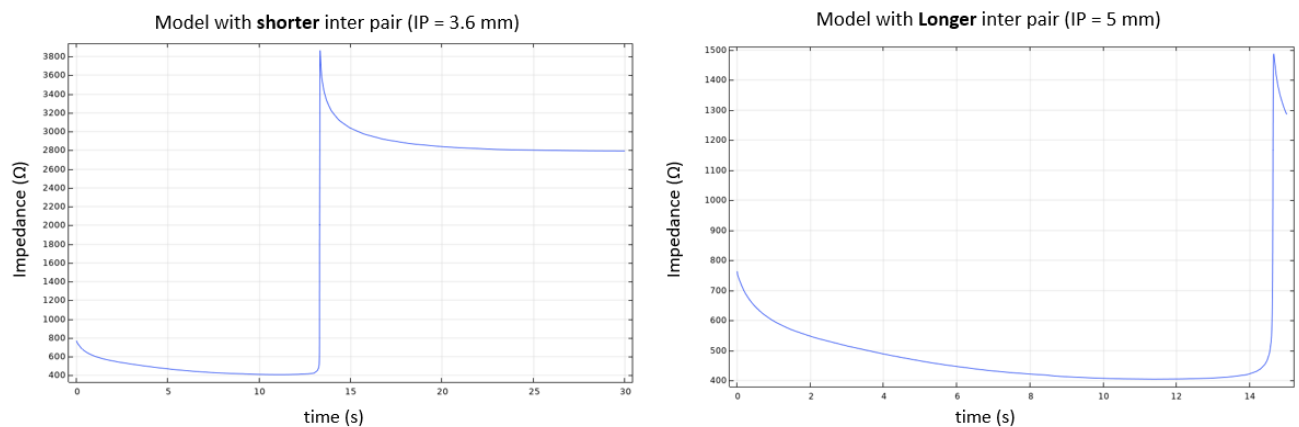


Figure 11: Simulated changes in tissue impedance during heating for two models with different inter-pair spacing of 3.6 mm and 5 mm

The total ablation time was equal in both cases while maintaining the same power level, so inter-pair spacing variation did not make any visible changes in electrical results.

The impact of inter-pair spacing on ablation zone formation was investigated. Temperature maps including thermal damage contours are provided in **Figure 12** and **Figure 13**.

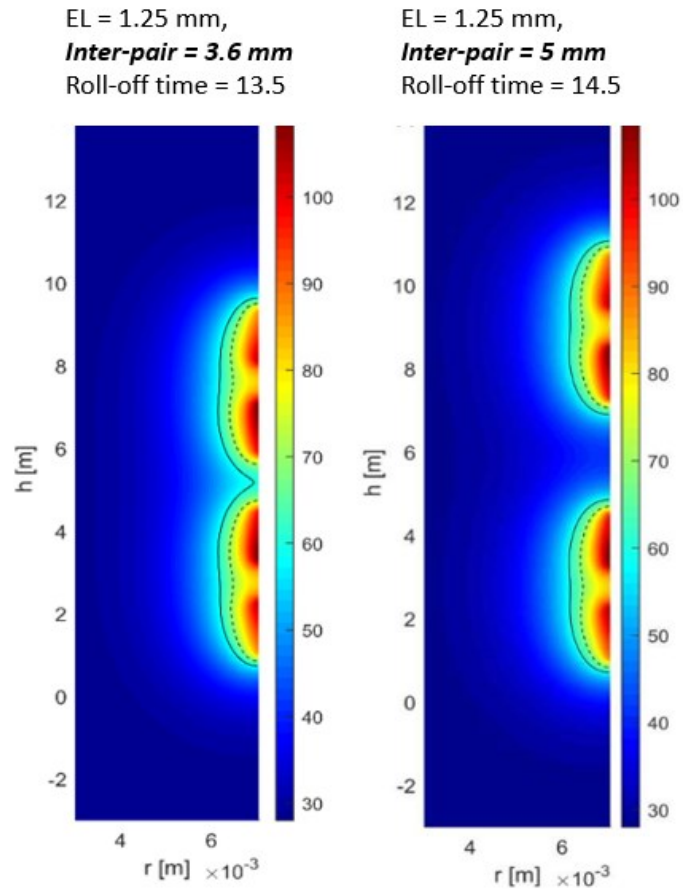


Figure 12: Simulated temperature maps illustrating ablation depth for two models with different inter-pair spacing of 3.6 mm and 5 mm

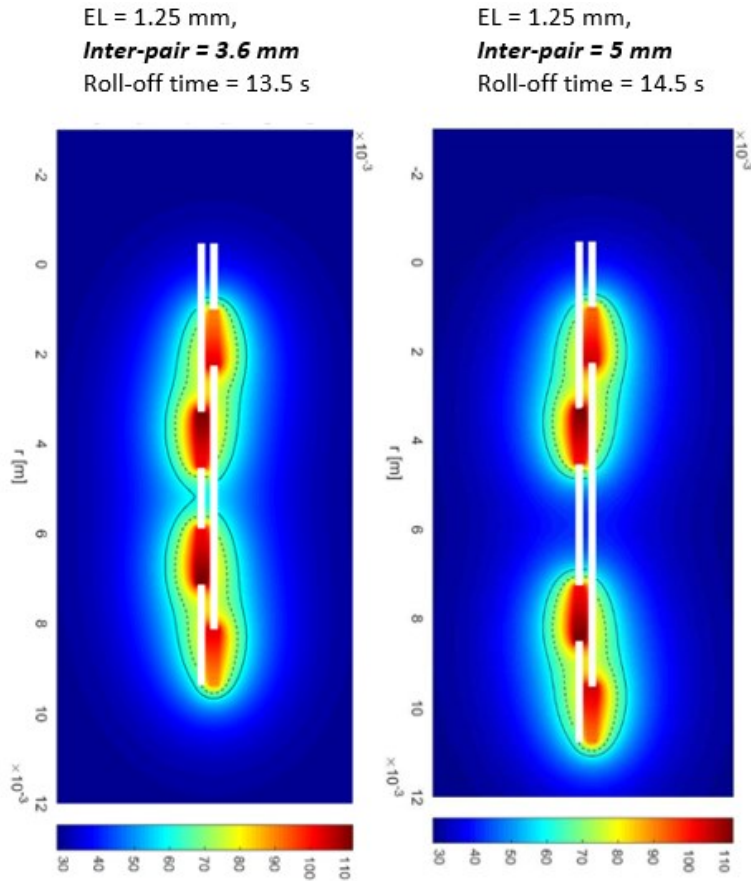
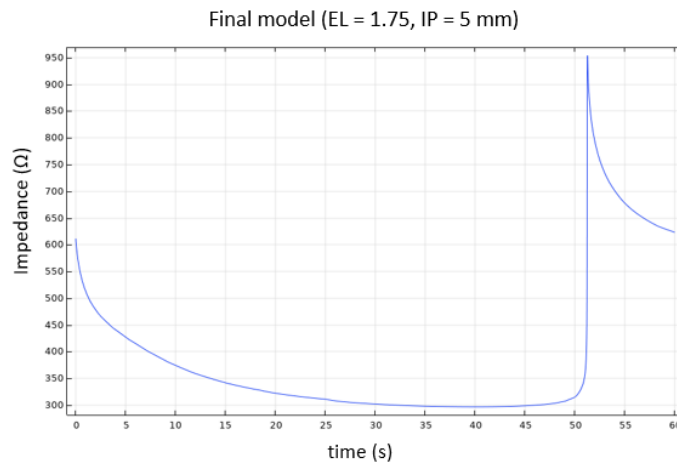


Figure 13: Simulated temperature maps illustrating surface ablation for two models with different inter-pair spacing of 3.6 mm and 5 mm

Simulated thermal results show a considerable difference in thermal lesion shapes both in depth and surface of the target tissue. There was a considerable separation in ablation zones when using a longer inter-pair which ends up in less surface burn while keeping the same ablation depth when compared to shorter inter-pair spacing. Depending on rhinitis specific treatment goals, utilizing longer inter-pair spacing can enhance the device performance during radiofrequency ablation by minimizing the continuity of the surface ablation.

## Suggested geometry

In order to sufficiently satisfy the treatment goals mentioned in chapter 2, a device model with a longer electrode length and longer inter-pair spacing was implemented. Longer electrode length can cause sufficient depth of ablation by delaying impedance roll-off. Also, longer inter-pair was chosen to inhibit undesired continuous surface ablation by increasing the distance between electrode pairs and consequently creating a more discrete pattern of ablation within the tissue surface. **Figure 14** illustrates the impedance behavior of recommended model.



*Figure 14: Simulated changes in tissue impedance during heating for the optimized model with electrode length of 1.75 mm and inter-pair spacing of 5 mm*

Simulation results indicates that inter-pair spacing variation can also impact the total ablation time. To be more precise, in cases were the ablation time is sufficiently long, inter-pair spacing can play a significant role in impedance roll-off time through thermal conductivity of tissue. The longer the inter-pair spacing is, the later the impedance roll-off happens, and vice versa. This is likely due to the fact that there would be larger volume of untargeted tissue between two

electrode pairs which if and only if the ablation time is long enough, thermal conductivity plays an important role in slowing the heating rate of the target tissue zones.

Temperature maps and thermal damage contour is shown below:

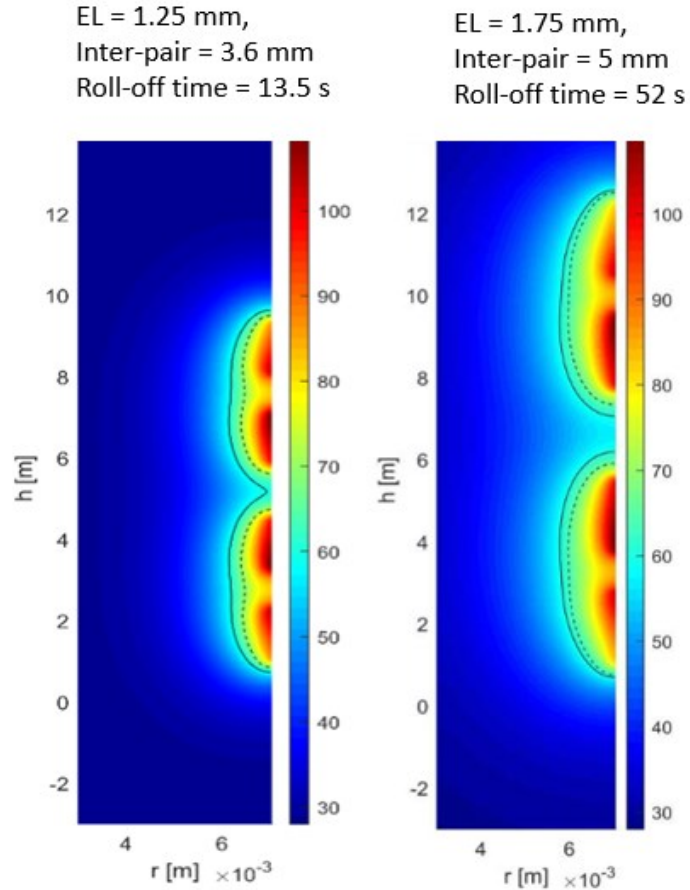


Figure 15: Simulated temperature maps illustrating ablation depth for two models with different sizes in electrode length and inter-pair spacing (base model with 1.25 mm electrode length and 3.6 mm inter-pair spacing, optimized model with 1.75 mm electrode length and 5 mm inter-pair spacing)

A larger ablation depth was observed with increasing inter-pair spacing and electrode length.

Both of the geometrical parameters were responsible for longer ablation time and larger ablation depth as described earlier.

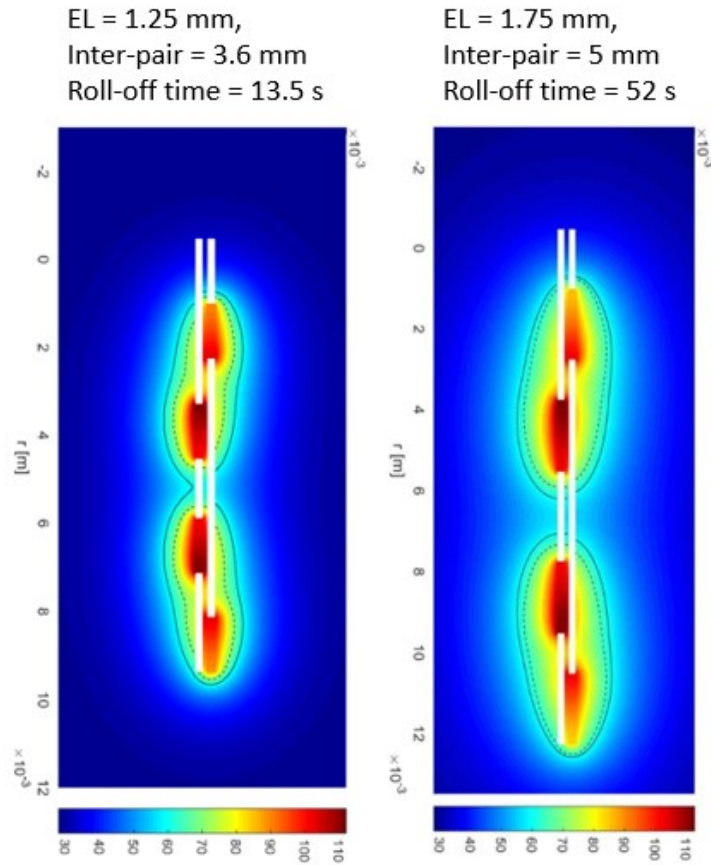


Figure 16: Simulated temperature maps illustrating surface ablation for two models with different sizes in electrode length and inter-pair spacing (base model with 1.25 mm electrode length and 3.6 mm inter-pair spacing, optimized model with 1.75 mm electrode length and 5 mm inter-pair spacing)

Finally, multi factor variation was simulated with longer electrode length and longer inter-pair to be compared with the first device. The model with longer electrode length and longer inter-pair spacing caused a considerable increase in ablation depth. Furthermore, it gave more control over tissue surface ablation due to causing more separation between ablation zones.

Summarized simulation findings are included in **Table 4** describing ablation results with regards to changes in single geometrical parameters of the RFA device.

Table 4: Summarized simulation findings

Condition	Parameter	Longer ablation depth	Longer surface ablation	Longer ablation time
Non-conditional	Longer electrode	+	+	+
Very short ablation time	Longer inter-pair	<i>Neutral</i>	-	<i>Neutral</i>
Sufficiently long ablation time	Longer inter-pair	+	-	+

Fast heating rates result in earlier impedance roll-off, which can decrease the effect of thermal conduction during radiofrequency ablation by limiting the heating duration. Thereby, Inter-pair spacing variation would not be as effective as when protocols with slower heating rates are applied during radiofrequency ablation. This is due to the fact that considerable heat is being transferred from hot regions to cooler regions in longer durations. Consequently, the impact of distance variation between electrode pairs on the ablation results can be considered as conditional.

Finally, optimized device geometry was recommended to Neurent Medical for manufacture with an electrode length of 1.75 mm and inter-pair spacing of 5 mm to guarantee a sufficiently large ablation depth for destruction of engorged mucous membrane within the nasal cavity.

## Chapter 4- Model verification through experiments

In order to validate the simulation results, *ex vivo* experiments were conducted with a similar RFA device on fresh bovine liver tissue obtained from a local slaughterhouse. The liver tissue was preheated up to 28-29 °C in the water bath before RF ablation. Different power levels was applied in experiments, and each protocol was involved with 3 trials for reliability purposes. Two RFA devices reflecting the same geometry as in the models were used in this study. Each device was consisted of 6 petals as shown in **Figure 17**.

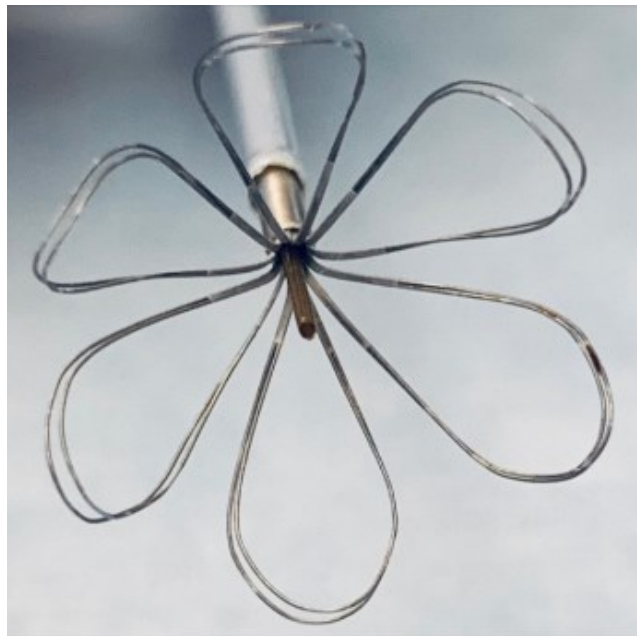


*Figure 17: Neurent Medical deployable RFA device consisting of 6 petals*

Each petal contains two parallel active and ground wires where four to five pairs of hemicylindrical electrodes were placed on them. The CAD module for a single petal in the RFA device, as well as experimental setup including RF generator, relevant mux boards, and profile builder system utilized in this work, are shown in **Figure 18** and **Figure 19**.

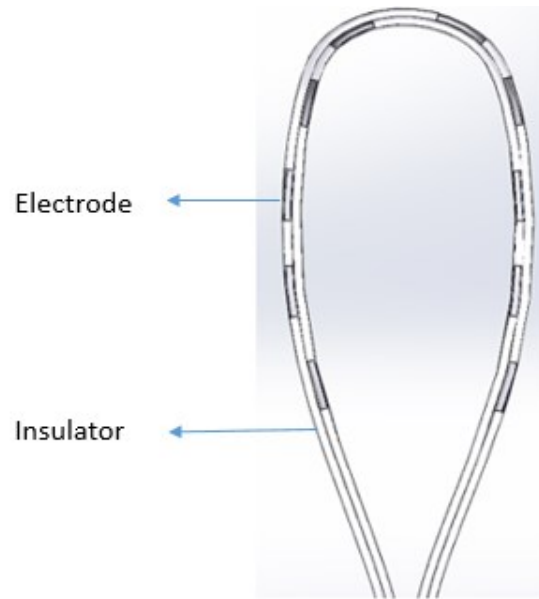


Figure 18: CAD illustration for a single petal of the Neurent device containing 5 pairs of electrodes (Image courtesy Neurent Medical)

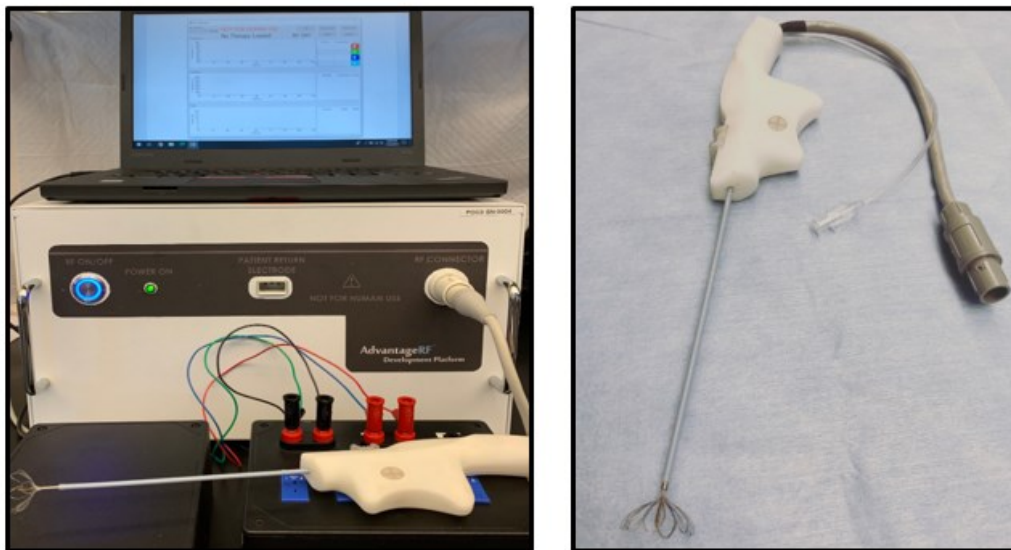


Figure 19: Experimental setup of radiofrequency ablation including utilized generator and the Neurent device

**Table 5** shows experimentally applied heating protocols in this work for model verification purpose. Two RFA devices have been tested with different geometrical parameters.

*Table 5: Table of heating protocols for constant power application- Ex vivo experiments*

<b>RFA device</b>	<b>Dimensions</b>	<b>Power level</b>	<b>Trials</b>
First device	EL = 1.25 mm Inter pair = 3.6 mm Electrode pairs = 5	2.5 W – 3 W	3
Second device	EL = 1.75 mm Inter pair = 5 mm Electrode pairs = 4	2.5 W – 3 W	3

Experimental results are provided in **Figure 20** indicating ablation times for both RFA devices with respect to power level.

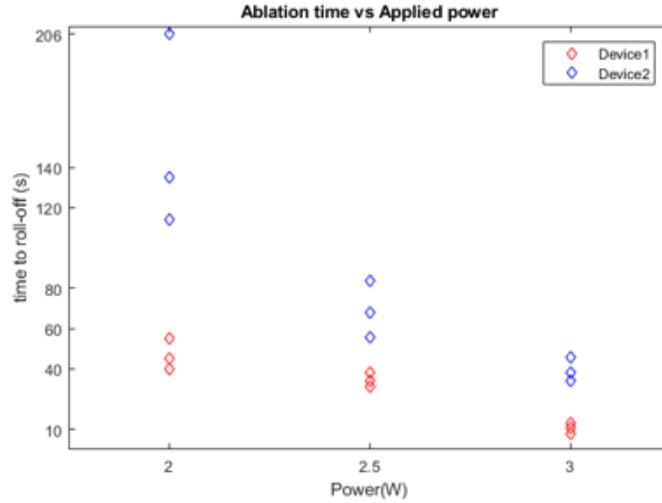


Figure 20: Experimental results illustrating impedance roll-off time for two Neurent devices with different geometrical parameters (Blue diamonds and red diamonds represent the performance of optimized device and base device, respectively)

As shown in the **Figure 20**, significant delay is visible when using an RFA device with longer electrode length and longer inter-pair. The potential reason could be the fact that larger volume of tissue would be involved in the target zone which might increase the effect of thermal conductivity. Moreover, according to simulation results, longer inter-pair can result in a cooler adjacent tissue outside of target zones when it is compared to the device with shorter dimensions. This could be an advantage to transfer the heat from target zones to adjacent cooler locations through thermal conduction within a longer period until impedance roll-off happens.

Also, ablation zones both from depth and surface standpoint are described in **Figure 21**. These measurements are based on macroscopically whitened zones of target tissue following RFA.

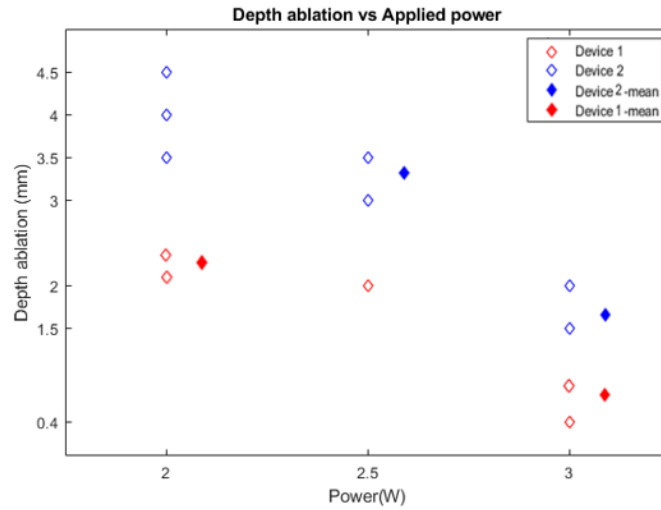


Figure 21: Experimental results showing ablation depth for two Neurent devices with different geometrical parameters (Blue diamonds and red diamonds represent the performance of optimized device and base device, respectively)

Ablation zones when using device 2 are considerably large compared to ablation zones created by device 1. This is because of more energy delivery through the target tissue. According to experimental results, mean depth of ablation for 2 watts applied power increased almost 2 mm to 4 mm when changing the device geometry from device 1 to device 2.

Experimental results were in consistency with computation results since the similar behavior of target tissue under different circumstances was noticed. Considerable increase in ablation time and lesion zones was observed when using devices with longer electrodes and longer inter-pair spacing as shown in **Figure 22**.

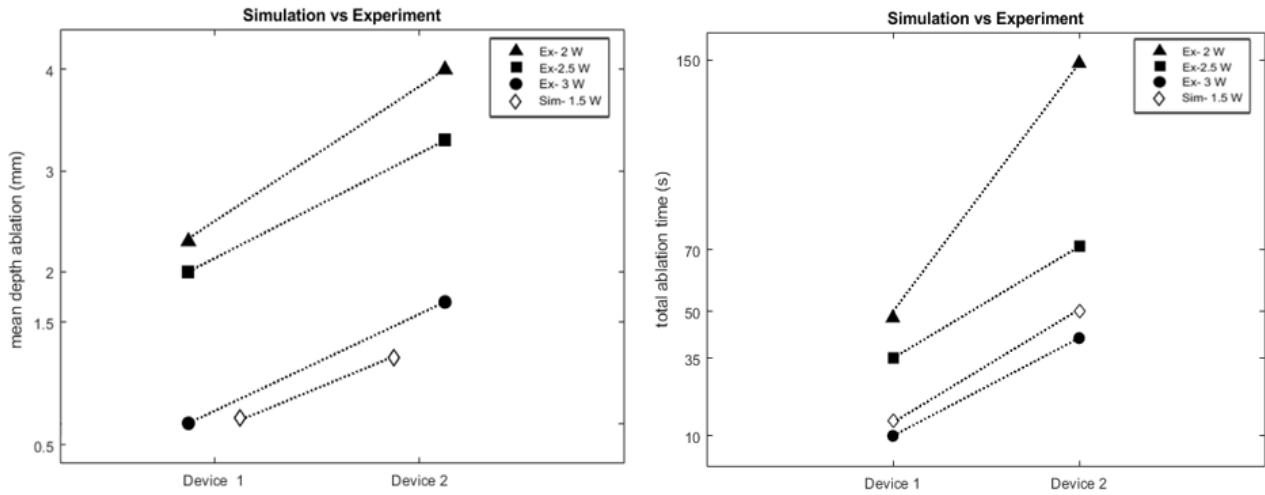


Figure 22: Simulation results vs Experimental results (Performance of device 1 with electrode length of 1.25 mm and inter-pair spacing of 3.6 mm, was compared to performance of device 2 with longer electrode length of 1.75 mm and longer inter-pair spacing of 5 mm)

There was a discrepancy regarding precise matching between simulation results and experimental results. Simulation results show a more severe heating than what happens in experiment, and thereby resulted in an earlier impedance roll-off even with a lower power level. This explains why ablation zones in simulation results are smaller in size compared to ablation zones in experimental results.

**Figure 23** demonstrates the differences in electrical parameters between experimental results and simulation results for device 1.

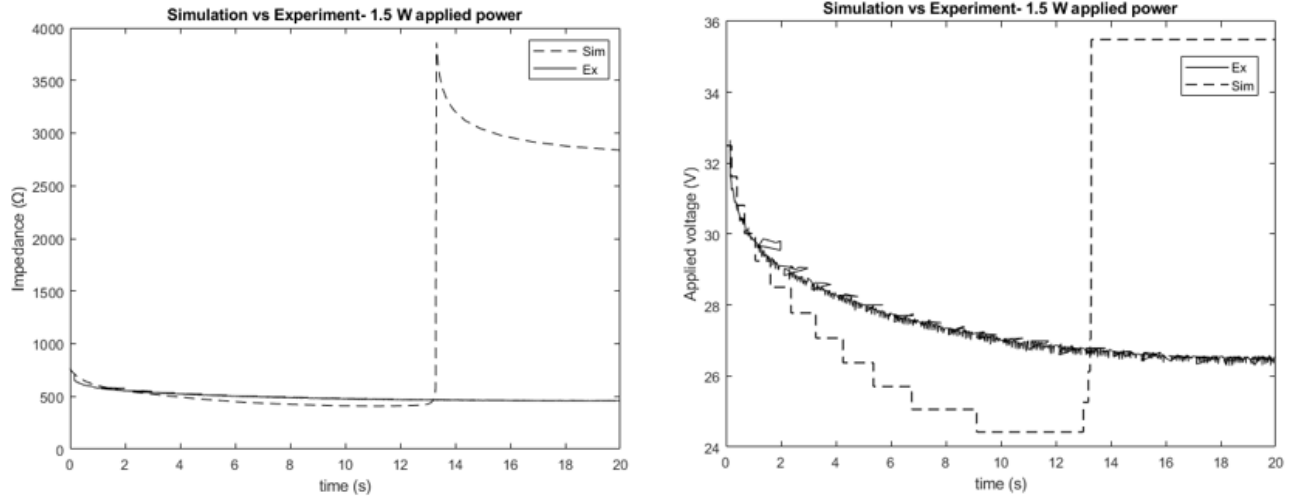


Figure 23: Changes in electrical parameters during heating in both simulation and experiment

Although initial electrical parameters (applied voltage of 33 V in simulation with respect to 1.5 W constant power level), matches with initial electrical parameters in experimental data, they were not remained equal during the ablation time. Consequently, impedance roll-off happened earlier in simulation results compared to experimental results. However, the model can be utilized as a useful tool to predict changes in ablation results with regards to variation in geometrical parameters of the device.

Depending on specific treatment needs in rhinitis treatment, it might not be ideal to experience tissue surface damage due to related complications following treatment such as bleeding and tissue desiccation within nasal cavity. However, causing a larger ablation depth was associated with also a larger surface ablation likely due to thermal conductivity impact in longer ablation times. **Figure 24** can shed light on this fact, demonstrating the setup and ablation zone photos following RFA on *ex vivo* liver tissue.

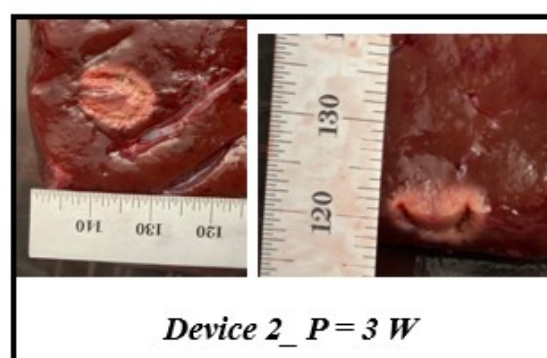
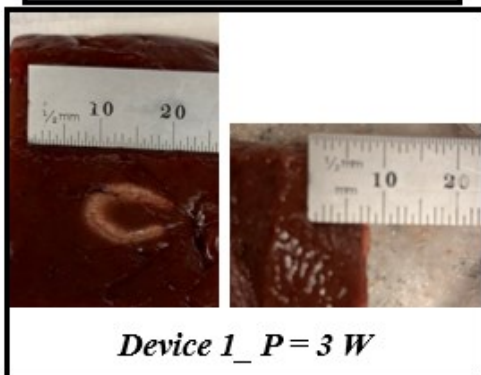
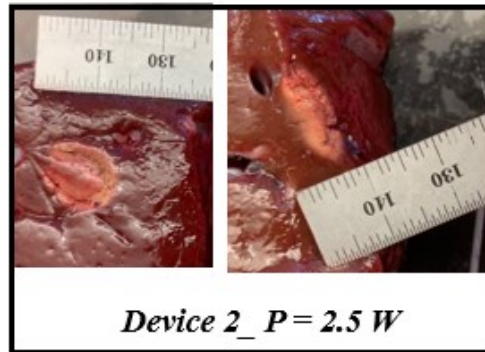
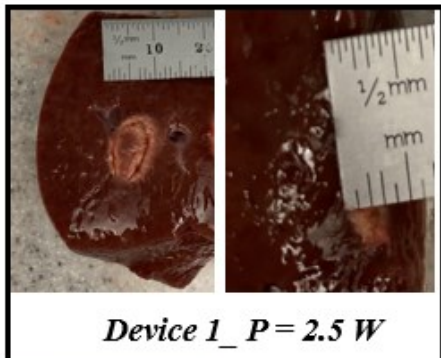
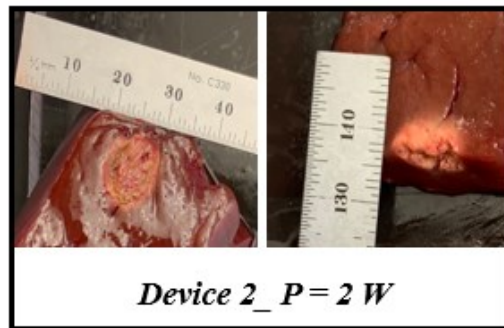
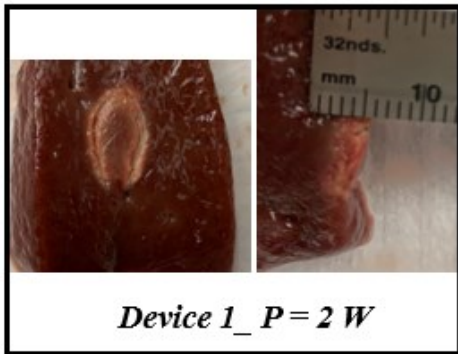
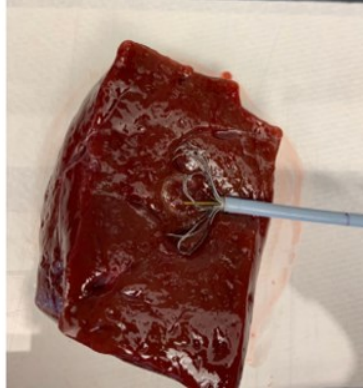


Figure 24: Thermal ablation zones following ex vivo experiments for device 1 (base device) and device 2 (optimized device with longer electrode length and longer inter-pair spacing)

Although applying higher power levels may decrease tissue surface damage as they tend to impede out faster, it still could not fulfill the primary purpose that is achieving sufficient depth of ablation. On the other hand, lower power levels can lead to a much longer ablation time that either cause a small ablation depth (if the power level is significantly low) or even very large thermal lesions which is indeed accompanied with significant surface burn. Therefore, with respect to specific treatment goals, in next chapter simulation results regarding considering the impact of blood perfusion during in vivo RFA are provided. Moreover, experimental results regarding the effects of different energy delivery strategies on ablation results will be discussed.

## Chapter 5- Assessment of blood perfusion and energy delivery strategies during radiofrequency ablation

This chapter describes the possible impact of different factors that might contribute to impact ablation results including blood perfusion, and pulsed energy delivery obtained through computation results and experiments, respectively.

### Blood perfusion impact

RFA success rate may be affected by multiple factors. Of those, blood perfusion within tissue is a puzzling variable that can have an inverse relationship with the created ablation zones <sup>32</sup>.

Evaluating the effect of blood perfusion might not be convenient through experiments due to the need for blood flow within target tissue. Therefore, computation results was done to comprehensively understand the contribution of blood flow in ablation results.

**Figure 25** compares simulation results between two similar models; one with taking into account the blood perfusion effect, and one considering no blood flow within the target tissue.

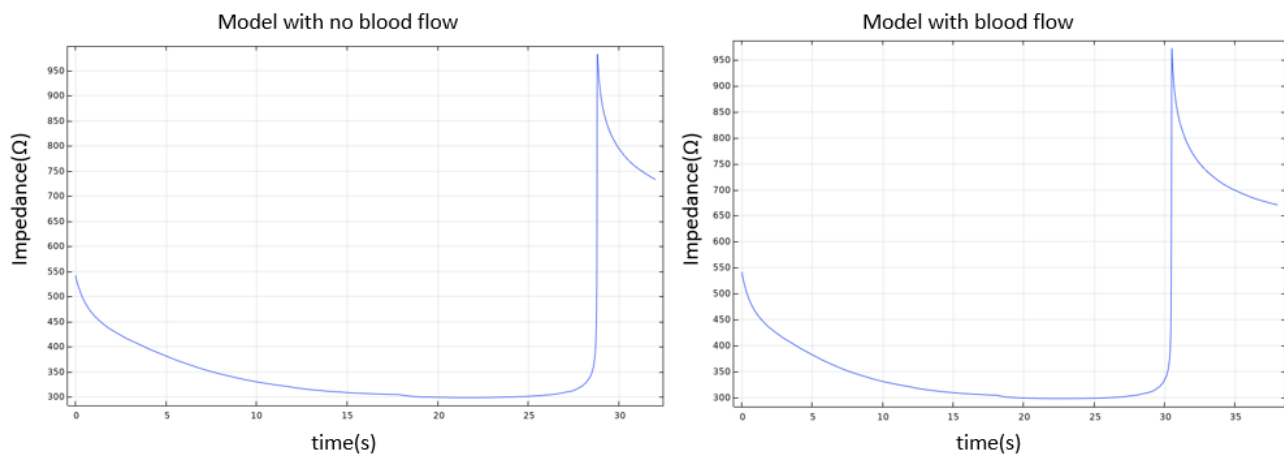
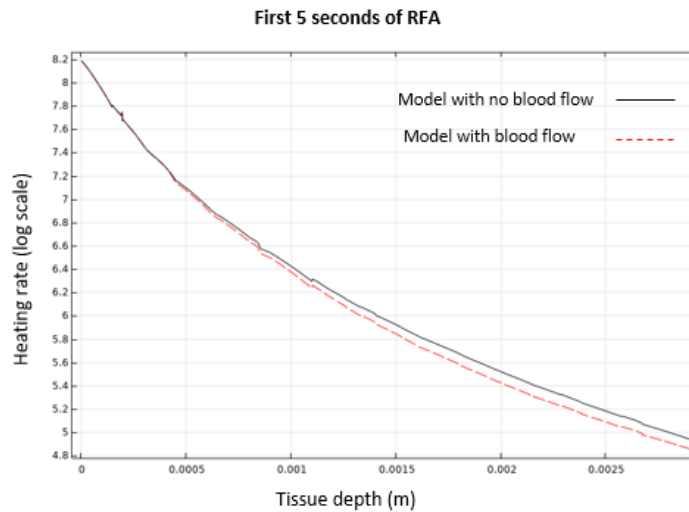


Figure 25: Simulated changes in tissue impedance for two models with and without blood flow

There was a very small difference in the ablation time, leading to same lesion size for both models. As demonstrated in **Figure 25**, impedance roll off happened in 31 seconds, and 28 seconds respectively in the model with and without existence of blood perfusion. This is likely due to the heat sink effect of blood flow carrying away the heat, and prolonging the ablation time. However, due to a very quick temperature rise in the regions proximal to electrodes, coagulation happened at the beginning of ablation leaving that part of tissue devoid of perfusion cooling effect, hence, behaving similar to the model with no blood flow. **Figure 26** demonstrates the heating rate behavior of both models in different times.



*Figure 26: Simulation results illustrating blood flow effect on tissue heating rate*

During the first few seconds of ablation, in locations close to the electrodes (less than 0.5 mm), coagulation immediately suppressed blood flow in those regions, and consequently both models experienced quite similar heating rates. Temperature value in these superficial regions did not have sufficient amount of time to stay below ablating temperatures and experience blood perfusion cooling effect, hence, leading to blood occlusion in a short ablation time.

## Pulsed energy delivery

Due to rhinitis specific treatment goals, impact of pulsed energy delivery on lesion zone formation was evaluated. This was done through conducting *ex vivo* experiments on liver tissue. The ablation zones both from depth and surface standpoint were then compared with when constant power was applied. Table below shows the applied heating protocols conducted with device 1.

*Table 6: Table of heating protocols for pulsed and constant energy deliveries- Ex vivo study*

Power (W)	Duty cycle %	Period (s)	Trials	Initial temperature (°C)
2	Constant	–	3	23
2	30	8	3	23
2	60	15	3	23
2	30	8	3	23
2	60	15	3	23
3	Constant	–	3	23
3	30	8	3	23
3	60	15	3	23
3	30	8	3	23
3	60	15	3	23

As shown in **Table 6**, power levels of 2 watts and 3 watts were chosen when using device 1. The impact of pulsed energy delivery on ablation results was assessed. **Figure 27** and **Figure 28**

show the created lesion sizes from depth and surface standpoints, respectively. After 120 seconds, the generator was turned off meaning end of treatment.

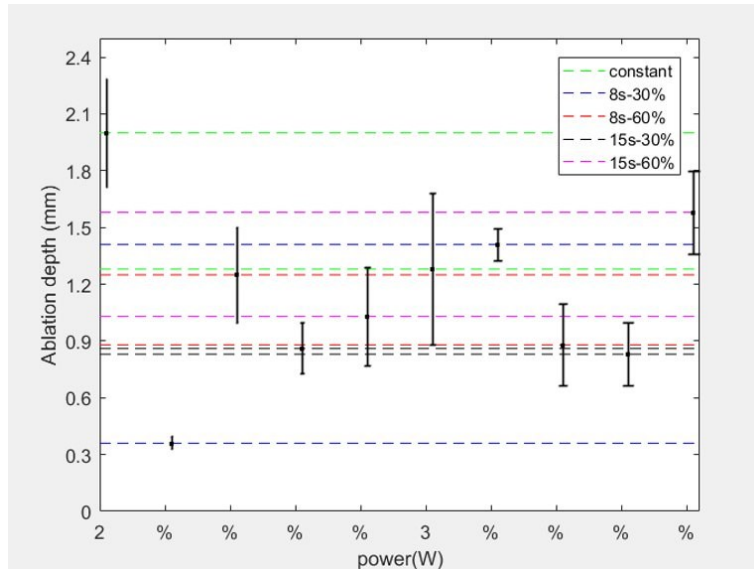


Figure 27: Experimental results showing ablation depth for both pulsed energy delivery and constant power application

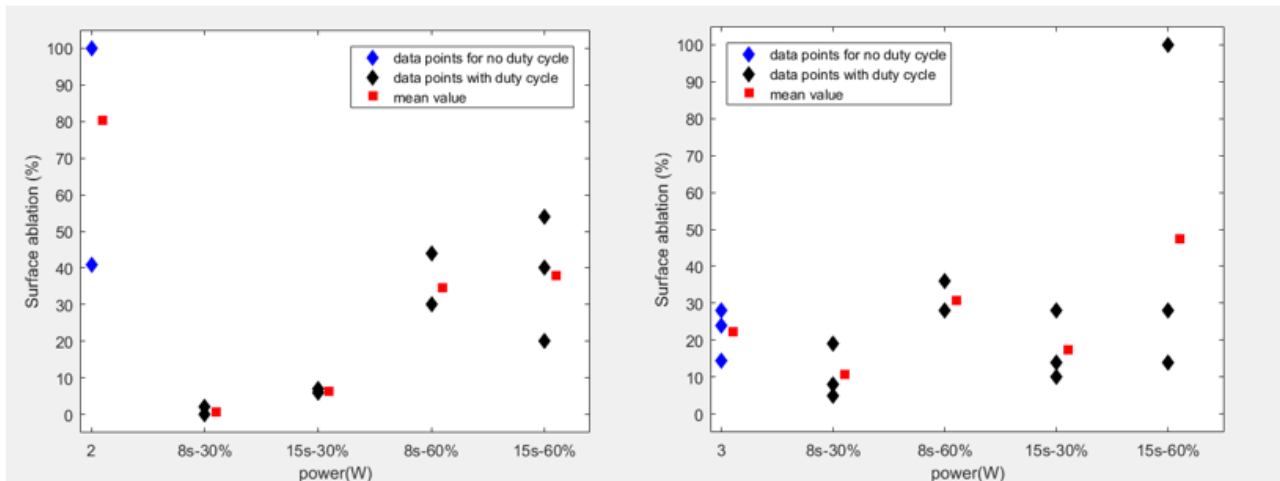


Figure 28: Experimental results showing surface ablation for both pulsed energy delivery and constant power application

Duty cycle application resulted in either increase or decrease in depth of ablation depending on applied power level. Unwanted surface damage was larger when larger ablation depth was achieved and vice versa. Surface and depth of ablations both decrease in size from constant power of 2 watts to 60% duty cycle and then to 30% duty cycle application. However, in the case of 3 watts applied power, lesions increased both in depth and surface when heating protocols changed from constant power application to 30% and 60% duty cycle applications.

## Chapter 6- Conclusions

A computational model was created to predict thermal ablation zones and transient impedance profiles during radiofrequency ablation for treating rhinitis. Simulation results predicted a prolonged impedance roll-off time from 13 s to 36 s followed by larger ablation zones when increasing the electrode length from 1.25 mm to 1.75 mm. Inter-pair spacing variation between electrode pairs can prolong ablation time depending on the applied power level and device geometry while at the same time impacting continuity of the surface thermal damage.

Moreover, simulation results indicated that, blood flow might not affect the ablation results when fast heating rates are applied due to quick temperature rise and instant cell death during radiofrequency ablation.

*Ex vivo* experiments were conducted to evaluate the impact of pulsed energy delivery on ablation results. Experimentally, achieving larger ablation depths was associated with larger tissue surface ablation. Therefore, minimizing surface damage through pulsed energy delivery may lead to smaller ablation depths that may not fulfill the primary treatment goal of rhinitis, i.e., achieving an ablation depth of 4 mm.

There were some limitations regarding the accuracy of the model. Simulated ablation zones were smaller, with a faster impedance roll-off when compared to *ex vivo* ablation results on the same tissue. This is probably due to the fact that electro-thermal properties of the target tissue implemented in the model from literature, were not precisely optimized for the specific experimental setup used in this study.

One potential variable that could have caused this discrepancy is tissue electrical conductivity function implemented in the model that was obtained from the literature. Unfortunately, there are

not a sufficient number of studies regarding tissue dielectric properties measurements taking into account varying heating rates within the target tissue, and thereby, introduced electro-thermal properties might not accurately describe a realistic behavior of ablated tissue. It would be beneficial to conduct more investigations regarding material properties of the tissue within the radiofrequency range at a variety of heating rates.

## References

1. Sin, B. & Togias, A. Pathophysiology of allergic and nonallergic rhinitis. *Proc. Am. Thorac. Soc.* **8**, 106–114 (2011).
2. Sur, D. K. & Scandale, S. Treatment of allergic rhinitis. *South Afr. Fam. Pract.* 398–403 (2010).
3. Skoner, D. P. Allergic rhinitis: Definition, epidemiology, pathophysiology, detection, and diagnosis. *J. Allergy Clin. Immunol.* **108**, S2–S8 (2001).
4. Scarupa, M. D. & Kaliner, M. A. Nonallergic Rhinitis, With a Focus on Vasomotor Rhinitis Clinical Importance, Differential Diagnosis, and Effective Treatment Recommendations. *World Allergy Organ. J.* **2**, 20 (2009).
5. Aoishi, K. *et al.* Treatment of allergic rhinitis with intranasal infusion of botulinum toxin type A in mice. *Life Sci.* **147**, 132–136 (2016).
6. Blaiss, M. S. Allergic rhinitis: Direct and indirect costs. *Allergy Asthma Proc. Provid.* **31**, 375–80 (2010).
7. Sur, D. K. C. & Plesa, M. L. Chronic Nonallergic Rhinitis. *Am. Fam. Physician* **98**, 171–176 (2018).
8. Weber, R. K. Nasal packing and stenting. *GMS Curr. Top. Otorhinolaryngol. Head Neck Surg.* **8**, (2011).
9. Radiofrequency ablation for pain. Available at: [http://www.mayfieldclinic.com/pe-rf\\_ablation.htm](http://www.mayfieldclinic.com/pe-rf_ablation.htm). (Accessed: 31st July 2019)
10. Curley, S. A. Radiofrequency Ablation of Malignant Liver Tumors. *Ann. Surg. Oncol.* **10**, 338–347 (2003).
11. McGahan, J. P. *et al.* Hepatic Ablation with Use of Radio-Frequency Electrocautery in the Animal Model. *J. Vasc. Interv. Radiol.* **3**, 291–297 (1992).
12. Brace, C. Thermal Tumor Ablation in Clinical Use. *IEEE Pulse* **2**, 28–38 (2011).
13. Chang, I. A. & Nguyen, U. D. Thermal modeling of lesion growth with radiofrequency ablation devices. *Biomed. Eng. OnLine* **3**, 27 (2004).
14. Kezirian, E. J., Powell, N. B., Riley, R. W. & Hester, J. E. Incidence of Complications in Radiofrequency Treatment of the Upper Airway. *The Laryngoscope* **115**, 1298–1304 (2005).
15. Osaki, Y. *et al.* Clinical effectiveness of bipolar radiofrequency ablation for small liver cancers. *J. Gastroenterol.* **48**, 874–883 (2013).

16. Rathke, H. *et al.* Comparison of four radiofrequency ablation systems at two target volumes in an ex vivo bovine liver model. *Diagn. Interv. Radiol.* **20**, 251–258 (2014).
17. Song, Y. Rhinitis radiofrequency ablation: FEM analysis and experiments, *MS Thesis, Department of Electrical and Computer Engineering, Kansas State University*, (2018).
18. Wang, X., Gao, H., Wu, S., Bai, Y. & Zhou, Z. RF ablation thermal simulation model: Parameter sensitivity analysis. *Technol. Health Care* **26**, 179–192 (2018).
19. Wang, X. *et al.* Numerical evaluation of ablation zone under different tip temperatures during radiofrequency ablation. *Math. Biosci. Eng.* **16**, 2514–2531 (2019).
20. Tian, Z., Dong, T., Cheng, Y., Hu, J. & Nan, Q. A Treatment Planning of Radio Frequency Ablation for Spinal Tumor. *Int. J. Comput. Methods* **16**, 1842005 (2018).
21. Trujillo, M. & Berjano, E. Review of the mathematical functions used to model the temperature dependence of electrical and thermal conductivities of biological tissue in radiofrequency ablation. *Int. J. Hyperthermia* **29**, 590–597 (2013).
22. Berjano, E. J. Theoretical modeling for radiofrequency ablation: state-of-the-art and challenges for the future. *Biomed. Eng. OnLine* **5**, 24 (2006).
23. Labonte, S. Numerical model for radio-frequency ablation of the endocardium and its experimental validation. *IEEE Trans. Biomed. Eng.* **41**, 108–115 (1994).
24. Sebek, J., Albin, N., Bortel, R., Natarajan, B. & Prakash, P. Sensitivity of microwave ablation models to tissue biophysical properties: A first step toward probabilistic modeling and treatment planning. *Med. Phys.* **43**, 2649–2661 (2016).
25. Deas, D., Gilart González, F., Troyen, D. & Vandenbosch, G. *Modeling of RF thermal ablation taking into account the temperature dependence of the tissue properties.* **40**, (2018).
26. Shao, Y. L., Leo, H. L. & Chua, K. J. Studying the thermal performance of a bipolar radiofrequency ablation with an improved electrode matrix system: In vitro experiments and modelling. *Appl. Therm. Eng.* **116**, 623–635 (2017).
27. Hall, S. K., Ooi, E. H. & Payne, S. J. Cell death, perfusion and electrical parameters are critical in models of hepatic radiofrequency ablation. *Int. J. Hyperthermia* **31**, 538–550 (2015).

28. Haemmerich, D., Santos, I. dos, Schutt, D. J., Webster, J. G. & Mahvi, D. M. In vitro measurements of temperature-dependent specific heat of liver tissue. *Med. Eng. Phys.* **28**, 194–197 (2006).
29. Haemmerich, D. & Webster, J. G. Automatic control of finite element models for temperature-controlled radiofrequency ablation. *Biomed. Eng. OnLine* **4**, 42 (2005).
30. Jain, M. K. & Wolf, P. D. Finite element analysis predicts dose-response relationship for constant power and temperature controlled radiofrequency ablation. in *Proceedings of the 19th Annual International Conference of the IEEE Engineering in Medicine and Biology Society. 'Magnificent Milestones and Emerging Opportunities in Medical Engineering'* (Cat. No.97CH36136) **1**, 165–168 vol.1 (1997).
31. Jain, M. K. & Wolf, P. D. Temperature-controlled and constant-power radio-frequency ablation: what affects lesion growth? *IEEE Trans. Biomed. Eng.* **46**, 1405–1412 (1999).
32. Dodd, G. D., Dodd, N. A., Lanctot, A. C. & Glueck, D. A. Effect of Variation of Portal Venous Blood Flow on Radiofrequency and Microwave Ablations in a Blood-perfused Bovine Liver Model. *Radiology* **267**, 129–136 (2013).